

A Distinct Class of Bursting Neurons with Strong Gamma Synchronization and Stimulus Selectivity in Monkey V1

Highlights

- A distinct neuron type with thin spikes and high burst propensity in monkey V1
- These neurons are present in both Old World and New World monkeys, but not in mice
- They show relatively strong gamma (30–80 Hz) rhythmicity and stimulus selectivity
- Firing suppression contributes to their orientation tuning and gamma rhythmicity

Authors

Irene Onorato,
Sergio Neuenschwander,
Jennifer Hoy, ..., Christopher Niell,
Wolf Singer, Martin Vinck

Correspondence

martin.vinck@esi-frankfurt.de

In Brief

Onorato et al. find a specialized V1 neuron type that has narrow-spike waveforms, fires in high-frequency bursts, is strongly phase locked to 30- to 80-Hz oscillations, and is highly stimulus-selective. This neuron class is found in both Old World and New World monkeys, but not in mice.

A Distinct Class of Bursting Neurons with Strong Gamma Synchronization and Stimulus Selectivity in Monkey V1

Irene Onorato,^{1,2} Sergio Neuenschwander,^{3,5} Jennifer Hoy,⁷ Bruss Lima,³ Katia-Simone Rocha,⁵ Ana Clara Broggini,¹ Cem Uran,¹ Georgios Spyropoulos,^{1,2} Johanna Klon-Lipok,^{1,3} Thilo Womelsdorf,⁶ Pascal Fries,¹ Christopher Niell,⁷ Wolf Singer,^{1,3,4} and Martin Vinck^{1,8,*}

¹Ernst Strüngmann Institute (ESI) for Neuroscience in Cooperation with Max Planck Society, Frankfurt, Germany

²International Max Planck Research School for Neural Circuits, Frankfurt am Main, Germany

³Max Planck Institute for Brain Research, Frankfurt, Germany

⁴Frankfurt Institute for Advanced Studies, Frankfurt, Germany

⁵Brain Institute, Federal University of Rio Grande do Norte, Natal, Brazil

⁶Vanderbilt University, Nashville, TN, USA

⁷Institute of Neuroscience and Department of Biology, University of Oregon, Eugene, OR, USA

⁸Lead Contact

*Correspondence: martin.vinck@esi-frankfurt.de

<https://doi.org/10.1016/j.neuron.2019.09.039>

SUMMARY

Cortical computation depends on interactions between excitatory and inhibitory neurons. The contributions of distinct neuron types to sensory processing and network synchronization in primate visual cortex remain largely undetermined. We show that in awake monkey V1, there exists a distinct cell type (>30% of neurons) that has narrow-waveform (NW) action potentials and high spontaneous discharge rates and fires in high-frequency bursts. These neurons are more stimulus selective and phase locked to 30- to 80-Hz gamma oscillations than other neuron types. Unlike other neuron types, their gamma-phase locking is highly predictive of orientation tuning. We find evidence for strong rhythmic inhibition in these neurons, suggesting that they interact with interneurons to act as excitatory pacemakers for the V1 gamma rhythm. We did not find a similar class of NW bursting neurons in L2-L4 of mouse V1. Given its properties, this class of NW bursting neurons should be pivotal for the encoding and transmission of stimulus information.

INTRODUCTION

Cortical tissue contains different types of neurons, which can be distinguished based on molecular, electrophysiological, and histological markers (Batista-Brito et al., 2018; Moore et al., 2010; Rudy et al., 2011; Gentet, 2012; Markram et al., 2004). Interactions between the two main classes, excitatory (E) and inhibitory (I) neurons, govern sensory responses and the emergence of network oscillations and synchrony (Isaacson and

Scanziani, 2011; Wilson et al., 2018; Vinck et al., 2013b; Buzsáki and Wang, 2012; Kopell et al., 2000; Wang, 2010; Haider et al., 2010; Haider and McCormick, 2009). However, the nature of these E-I interactions in primate model systems remains largely undetermined.

The primary visual cortex is one of the most widely studied model systems of the nervous system. The response properties of V1 neurons, for example orientation tuning, have been extensively described in different species. Furthermore, many visual stimuli give rise to prominent fast “gamma” oscillations (30–80 Hz) in area V1 (Gray et al., 1989; Jagadeesh et al., 1992; Gray et al., 1990). The oscillatory synchronization of V1 spiking activity may determine how stimulus information is transmitted to higher brain areas (Fries, 2015; Womelsdorf et al., 2012; Salinas and Sejnowski, 2000; Singer and Gray, 1995; Abeles, 1982; Buzsáki, 2006). E-I interactions are thought to make major contributions to both V1 orientation tuning and gamma oscillations (Shapley et al., 2003; Buzsáki and Wang, 2012; Wang, 2010). Recent studies in rodents have begun to genetically target distinct cell types to study their precise contributions to sensory tuning and network oscillations. These studies support a role for inhibition in shaping orientation and direction selectivity of V1 neurons (Kerlin et al., 2010; Znamenskiy et al., 2018; Perrenoud et al., 2016). Furthermore, they have implied specific classes of inhibitory interneurons in the generation of V1 gamma oscillations in mice (Veit et al., 2017; Chen et al., 2017; Senzai et al., 2019; Perrenoud et al., 2016). Yet, rodents and primates differ greatly in the functional and anatomical organization of their cortices (Ohki and Reid, 2007) and their cognitive capacity. Further, monkey V1 shows gamma oscillations that are very strong as compared to other model systems such as monkey V4 and mouse V1 (Vinck and Bosman, 2016), suggesting that the nature of E-I interactions might be fundamentally different in monkey V1. It is thus critical to study the contributions of different cell types to sensory processing and synchronization in primate V1. In primate cortex, there are only

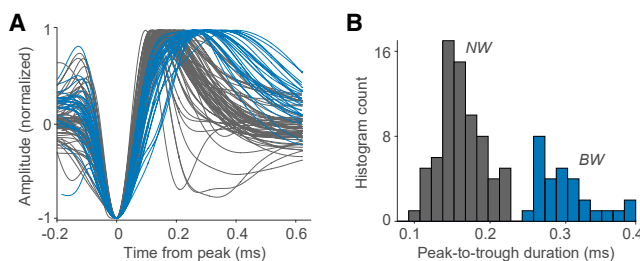


Figure 1. We Analyzed the Waveforms of Action Potentials (APs) to Distinguish between Broad-Waveform (BW) Neurons and Narrow-Waveform (NW) Neurons

(A) AP waveforms of the recorded neurons ($n = 100$ cells, two monkeys) as a function of time (ms). We normalized the waveforms between -1 and $+1$ and aligned them to their respective peaks. Gray and blue traces correspond to NW and BW APs, respectively.

(B) Histogram count of waveform peak-to-trough durations. The distribution of peak-to-trough durations was bimodal ($p < 0.05$; Hartigan's dip test).

limited possibilities to target cell types based on molecular markers. Primate studies have therefore analyzed action potential (AP) waveforms and firing statistics to distinguish between fast-spiking interneurons and excitatory cells, which generally yields high overlap with genetic and morphological markers of cell classes (McCormick et al., 1985; Senzai et al., 2019; Miri et al., 2018; Gentet et al., 2012; Cardin et al., 2009; Vinck et al., 2013a; Ardid et al., 2015; Mitchell et al., 2007; Vinck et al., 2016; Perrenoud et al., 2016; Hasenstaub et al., 2005; Nowak et al., 2003; Trainito et al., 2019). Furthermore, the differentiation between distinct excitatory cell types depends at present primarily on firing characteristics (Nowak et al., 2003; Barthó et al., 2004).

In the present study, we recorded spikes and local field potential (LFP) activity from awake macaque V1. We analyzed firing statistics and action-potential waveforms to distinguish between different cell classes. Fast-spiking interneurons and excitatory cells are commonly distinguished by their narrow-waveform (NW) and broad-waveform (BW) spikes, respectively (Senzai et al., 2019; McCormick et al., 1985; Csicsvari et al., 1999; Perrenoud et al., 2016). Yet, we observed that the percentage of NW neurons in macaque V1 largely exceeds the known percentage of GABAergic interneurons (Hendry et al., 1987). We show that NW neurons form two separate classes, distinguished by their propensity to fire burst-spikes. We then compare the stimulus-selectivity and rhythmic-synchronization properties among these two different NW and BW neurons.

RESULTS

We recorded spikes and LFPs from area V1 in two macaque monkeys (see **STAR Methods**). Simultaneous recordings were made from 2 to 10 single electrodes, which had distances to each other between 1 and 3 mm. We acutely inserted the electrodes on each recording day and typically positioned them in the superficial layers. During the recordings, we presented drifting-grating stimuli for a duration of 800–1,500 ms, while the monkeys performed a fixation task. The drifting gratings were centered on the receptive fields (RFs) of the recorded units

($\sim 8^\circ$ diameter circular aperture). We presented 16 different stimulus directions in a random order across trials. Note that statistical parameters are largely described in the figure captions.

Classification and Characterization of Neuron Types

We used semi-automatic spike sorting to isolate single units ($n = 100$ in two monkeys). We analyzed the waveforms of the APs to distinguish between NW and BW neurons (Figure 1; for estimates of wideband waveforms, see Figure S1). For each neuron, we computed the average AP waveform and its peak-to-trough duration (Figures 1A and 1B). The histogram of peak-to-trough durations was bimodal (Figure 1B). We refer to neurons with long (>0.235 ms) and short (<0.235 ms) peak-to-trough durations as BW ($n = 29$) and $n = 71$ neurons, respectively. The percentage of NW neurons was 71% (Figure 1). This replicates the findings of Gur et al. (1999), who observed a similar distribution in all layers of macaque primary visual cortex.

Which cell types do these NW and BW neurons correspond to? Previous studies have distinguished between fast-spiking interneurons and excitatory cells based on the peak-to-trough duration of the AP waveform. This approach is motivated by several considerations: (1) the percentage of inhibitory (GABAergic) interneurons in cortex is small (Hendry et al., 1987; Rudy et al., 2011); (2) inhibitory interneurons, especially fast-spiking interneurons, typically have NW APs (Vinck et al., 2016; Gentet et al., 2012; Senzai et al., 2019; Csicsvari et al., 2003; Miri et al., 2018; Perrenoud et al., 2016; Sirota et al., 2008; McCormick et al., 1985); (3) by contrast, most E neurons have BW APs (Senzai et al., 2019; Gentet et al., 2012; Vinck et al., 2016; Hasenstaub et al., 2005; Perrenoud et al., 2016; McCormick et al., 1985); and (4) in most systems, the percentages of NW neurons and inhibitory interneurons are comparable (Senzai et al., 2019; Vinck et al., 2016; Ardid et al., 2015; Miri et al., 2018; Csicsvari et al., 2003; Sirota et al., 2008). Various techniques, including optogenetics, have been used to validate the identification of neuron types based on AP waveform (Senzai et al., 2019; Miri et al., 2018; Vinck et al., 2016; Gentet et al., 2012; Vinck et al., 2016; Barthó et al., 2004). We recorded from single units in L2/3 and L4 of mouse V1. We found that the percentages of NW neurons in L2/3 and L4 are 9.2% and 7.4%, respectively, consistent with previous studies (Vinck et al., 2015; Niell and Stryker, 2010; Senzai et al., 2019; Vinck et al., 2016). Yet, in the case of area V1 in the macaque, the percentage of NWs that we observed ($\sim 70\%$) was much larger than the expected fraction (20%–25%) of GABAergic interneurons (Hendry et al., 1987). This implies that a substantial fraction of NW neurons in macaque V1 might be excitatory rather than inhibitory. Thus, the population of NW neurons should be heterogeneous.

We therefore asked whether this population can be subdivided into distinct neuron types. Neuron types can be identified based not only on the AP waveform but also on their characteristic firing patterns. Previous studies have shown that E and I neurons can be distinguished based on the autocorrelogram of the spike trains (Csicsvari et al., 2003). The autocorrelogram quantifies the likelihood that a neuron spikes at time $t + \tau$, given that it has spiked at time t . Fast-spiking interneurons typically reach a peak in the autocorrelogram at long time

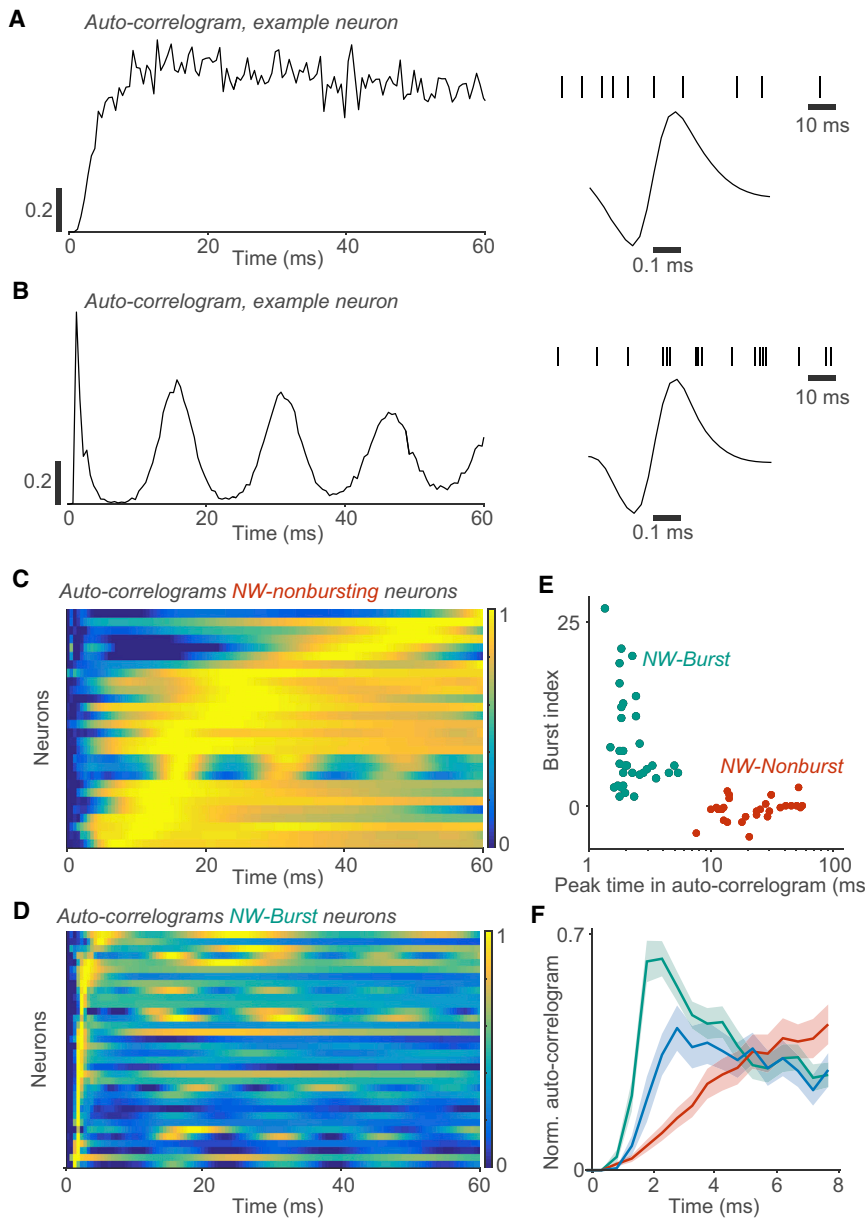


Figure 2. NW Neurons Formed Two Non-overlapping Clusters, which Were Distinguished by Their Bursting Propensity

(A) Example NW neuron. Left: autocorrelogram as a function of time. The autocorrelogram was normalized between 0 and 1 and computed for the visual stimulation period (>200 ms after stimulus onset). Right: action-potential waveform and an example spike train during visual stimulation.

(B) Similar to (A), but now for another example NW neuron.

(C) Autocorrelograms for NW-nonburst neurons. Each row represents one neuron. Shown are the polynomial fits to the autocorrelograms (see STAR Methods). The rows are sorted according to the time at which the smoothed autocorrelogram reached a global peak (see STAR Methods).

(D) Similar to (C), but now for NW-burst neurons.

(E) The time at which the autocorrelogram reached a global peak (within 60 ms) versus burst propensity (as a Z score). The burst-propensity measure was constructed by comparing the value of the autocorrelogram between short and long time delays (see STAR Methods).

(F) Mean autocorrelogram for each cell class as a function of time (ms). The autocorrelograms were normalized between 0 and 1 and then averaged across neurons. Shaded regions correspond to standard errors of the mean across neurons. Turquoise, red, and blue colors indicate NW-burst, NW-nonburst, and BW neurons, respectively.

delays >10 ms (Vinck et al., 2016; Csicsvari et al., 2003; Senzai et al., 2019; Barthó et al., 2004; Vinck et al., 2013a). This indicates that these neurons have a relatively long refractory period and do not engage in burst firing. A similar firing behavior can be observed in response to intracellular current injections (Gray and McCormick, 1996; Nowak et al., 2003). By contrast, E neurons often fire in bursts, which results in an early peak in the autocorrelogram (Csicsvari et al., 2003; Vinck et al., 2016; Nowak et al., 2003).

We used a similar approach and computed the autocorrelogram for each of the single neurons. For this purpose, we used the stationary part of the visual stimulus period (>200 ms after stimulus onset). We chose this period, because a large number of spikes are needed to reliably estimate the autocorrelogram.

We fitted polynomial functions to the autocorrelogram in order to determine the time at which it reached a global peak (see STAR Methods). In addition, we computed two measures of burst propensity by comparing the values of the autocorrelogram between short and long time delays (see STAR Methods). We found that NW neurons formed two separate clusters (Figures 2A–2E and S2; see STAR Methods). The first cluster of neurons (“NW-nonburst,” n = 28/100) had a late peak in the autocorrelogram

and did not engage in burst firing (Figures 2A and 2C–2E). These neurons had firing characteristics similar to those of fast-spiking interneuron (see Discussion). The second cluster of neurons (“NW-burst,” n = 34/100) had an early peak in the autocorrelogram and a high propensity to fire burst spikes with 2- to 4-ms inter-spike intervals (Figures 2A–2D and 3A). Similar firing patterns in NW neurons were observed in a New World capuchin monkey (Figures S3A and S3B). These characteristics of NW-burst neurons suggest that they are excitatory, like the BW neurons (Nowak et al., 2003) (we will further address this in the Discussion).

We performed the same analysis for recordings of L2/3 and L4 neurons in mouse V1 (see STAR Methods). We used the stationary part of the visual stimulus period during sitting epochs.

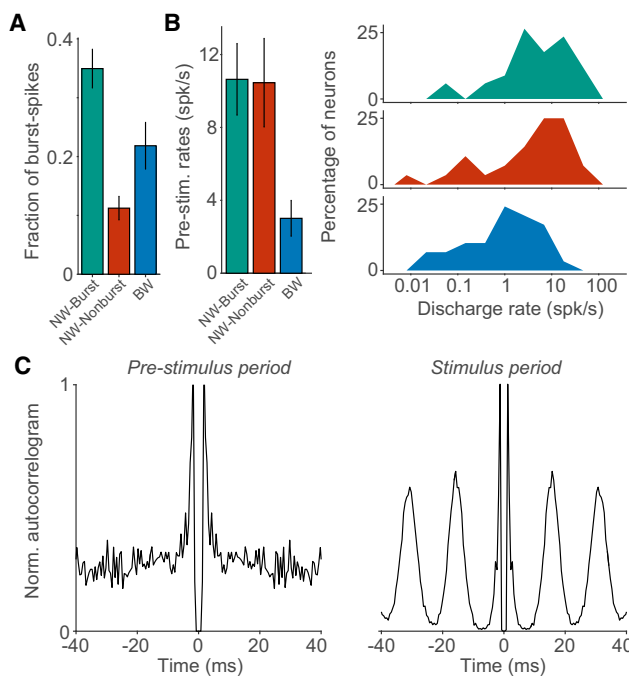


Figure 3. Differences between Neuron Types in Bursting Propensity and Discharge Rates

(A) Mean number of high-frequency burst spikes (subsequent spikes within 6-ms intervals) divided by the total number of spikes. This burst fraction was computed for the visual-stimulation period (>200 ms after stimulus onset). NW-burst neurons fired more burst spikes than the other neuron types (BW, $p < 0.005$; NW-nonburst, $p < 0.001$, permutation test). BW neurons fired more burst spikes than NW-nonburst neurons ($p < 0.05$, permutation test).

(B) Left: mean discharge rates (spikes/s) during the pre-stimulus period. Right: distribution of pre-stimulus discharge rates across neurons. Note that the discharge rates are shown on a logarithmic scale. NW-burst and NW-nonburst neurons had higher rates than BW neurons (NW-burst versus BW, $p < 0.005$; NW-nonburst versus BW, $p < 0.001$, permutation test). There was no significant difference between NW-burst and NW-nonburst neurons ($p > 0.05$, permutation test).

(C) Autocorrelograms for an example NW-burst neuron (same neuron as in Figure 2B). The autocorrelograms were computed both for the pre-stimulus (left) and the stimulus period (right). This neuron had a high burst propensity in both periods. For a correlation analysis, see Figure S5.

Error bars indicate SEs of the mean.

Thus, the behavioral conditions (drifting gratings and stationary) were comparable between mouse and macaque V1. A subset of the BW neurons showed burst firing, consistent with previous studies (Barthó et al., 2004; Vinck et al., 2016; Figures S4D and S4E). Using the same criterion of bursting as for NW-burst neurons, we found that there were 35% of burst-firing BW neurons in mouse L2/3, comparable to 52% of bursting BW neurons in macaque V1 (statistical difference not significant [n.s.], binomial test). In mouse L2/3 and L4, NW neurons showed late peaks in the autocorrelogram, and only one of the L2/3 neurons and one of the L4 NW neurons passed our criterion for NW-burst neurons, although these two neurons had a weak burst propensity compared to the NW-burst neurons in macaque V1 (Figures S4D and S4E). Thus, macaque V1 contains a large population of bursting NW neurons that is not found in mouse V1.

We further examined differences in the burst propensity and discharge rates among NW-burst, NW-nonburst, and BW neurons in macaque V1. Of the three neuron classes, NW-burst neurons had the highest burst propensity (Figures 2F and 3A). A substantial fraction of their spikes had inter-spike intervals shorter than 6 ms (~35%) and 3.5 ms (~25%) (Figures 3A and S5B). The first spike of the burst had a greater AP amplitude than the subsequent spikes in a burst ($p < 0.001$, t test). Conversely, NW-nonburst neurons rarely fired spikes within 3.5-ms intervals (Figure S5B). BW neurons had a higher burst propensity than NW-nonburst neurons (Figures 2F and 3A). Yet, the population of BW neurons was heterogeneous (Figure S2) and contained both bursting and nonbursting neurons (Figure S2A). Another defining characteristic of BW neurons was a low discharge rate (quantified in the pre-stimulus period) as compared to NW-burst and NW-nonburst neurons (Figure 3B), similar to mouse V1 (Figure S4C). NW-burst neurons and NW-nonburst neurons had similar discharge rates (Figure 3B).

Does the high burst-propensity of NW-burst neurons depend on visual stimulation, or do they also have a high burst propensity during spontaneous firing? To investigate this, we computed the autocorrelogram both for the visual stimulation and the pre-stimulus period. The burst propensity of NW-burst neurons was significantly correlated between the pre-stimulus and the stimulus period (Figures 3C and S5D). Their burst propensity did not significantly differ between the stimulus and pre-stimulus periods (Figure S5D). In fact, during the pre-stimulus period, NW-burst neurons still fired a large fraction of their spikes with inter-spike intervals shorter than 6 ms (Figure S5C). Thus, the high burst propensity of NW-burst neurons was not a consequence of visual stimulation and was also observed during periods of spontaneous firing.

Orientation Selectivity and Modulation by Grating Phase

We proceeded by comparing visual-response properties among the three classes of neurons. We first examined the tuning of discharge rates to the orientation and direction of the drifting-grating stimuli. For each neuron, we computed the orientation-selectivity index (OSI) and the direction-selectivity index (DSI; see STAR Methods). We found that NW-burst neurons were more orientation-tuned than NW-nonburst and BW neurons (Figure 4A; see Figure S6 for the two monkeys). By contrast, NW-nonburst neurons had the weakest orientation and direction selectivity of the three neuron types (Figures 4A and 4B). Thus, the three classes of neurons differed not only in their basic firing properties but also in their sensory selectivity.

Next, we determined the extent to which these neurons had simple or complex RFs. The distinguishing feature of simple V1 cells is that their firing is strongly modulated by the phase of grating stimuli (Martinez and Alonso, 2003). These cells are predominantly found in L4 (Martinez and Alonso, 2003). By contrast, the discharge rates of complex V1 cells are only weakly modulated by the phase of grating stimuli (Martinez and Alonso, 2003). These cells are mainly found in L2/3 and L5 (Martinez and Alonso, 2003). For each neuron, we estimated the discharge rate as a function of time by convolving

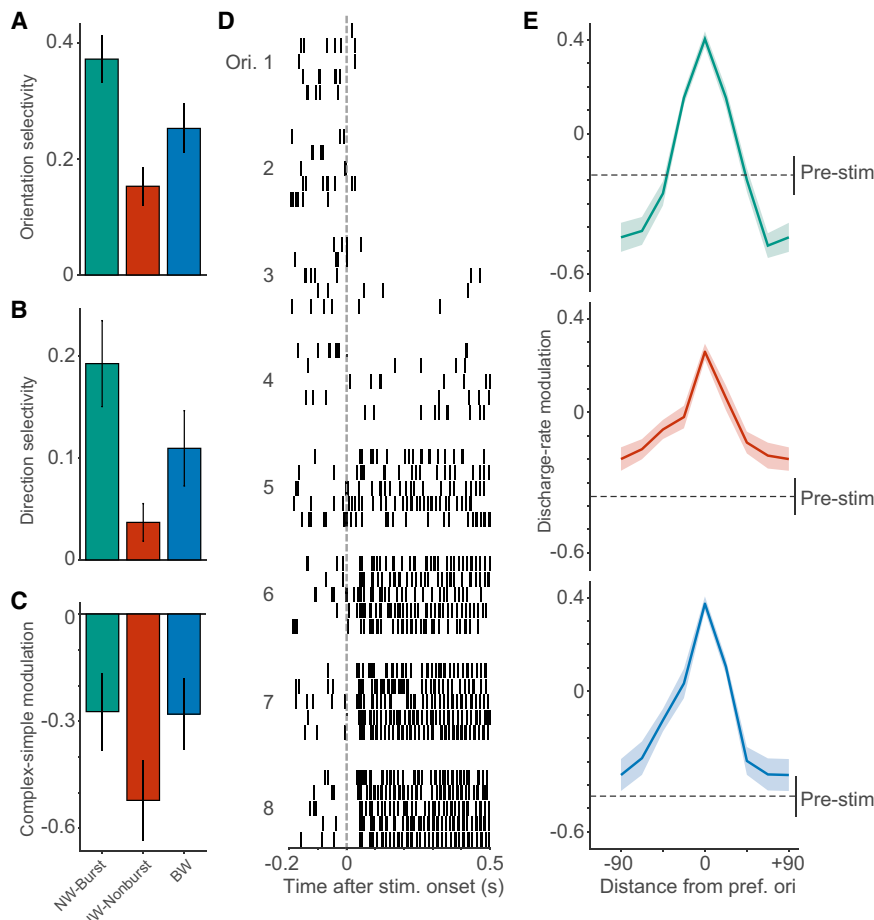


Figure 4. The Three Neuron Types Differed in Their Stimulus Selectivity

NW-burst neurons were most orientation-selective, and their discharge rates were suppressed for non-preferred stimulus-orientations.

(A) Mean orientation-selectivity index (OSI) for the three neuron types. NW-burst neurons had higher OSI values than NW-nonburst and BW neurons (NW-burst versus NW-nonburst, $p < 0.001$; NW-burst versus BW, $p < 0.05$, permutation test, see STAR Methods). BW neurons had higher OSI values than NW-nonburst neurons ($p < 0.05$).

(B) Mean direction-selectivity index (DSI). NW-burst and BW neurons had higher DSI values than NW-nonburst neurons ($p < 0.001$ and $p < 0.05$, respectively, permutation test; see STAR Methods). The DSI values of NW-burst and BW neurons did not show a significant difference ($p > 0.05$, permutation test).

(C) Mean simple versus complex cell modulation. This modulation was measured as $(F_1 - F_0)/(F_1 + F_0)$. The F_1 represents the modulation of a neuron's discharge rate by the phase of the drifting-grating (in spikes/s). The F_0 represents the increase in the mean discharge rate (in spikes/s). Values higher than zero indicate simple-cell receptive-field properties. BW neurons had higher modulation values than NW-nonburst neurons (BW versus NW-nonburst, $p < 0.05$, permutation test; see STAR Methods). NW-burst and NW-nonburst neurons did not significantly differ ($p > 0.05$, permutation test; see STAR Methods).

(D) Example NW-burst neuron (same neuron as in Figure 2B) We show the spike raster plots as a function of time (s) for each of the eight stimulus orientations. The orientations are sorted by the mean discharge rate. For each orientation, we show the first five stimulus trials.

(E) Mean discharge-rate modulation as a function of stimulus orientation. To compute this modulation, we first sorted orientations by the mean change in discharge rate. We then aligned the orientations to the preferred stimulus orientation. We computed the discharge-rate modulation as $(a - b)/(a + b)$. Here, a is either the discharge rate for one of the eight stimulus orientations or the discharge rate for the pre-stimulus period. The variable b represents the mean discharge rate across orientations. The dashed lines indicate the mean ± 1 SD for the pre-stimulus period. For NW-burst neurons, discharge rates for the pre-stimulus period were higher than for the four worst stimulus orientations ($p < 0.05$, two-sided t test). For NW-nonburst neurons, discharge rates were higher for the four worst stimulus orientations than the pre-stimulus period ($p < 0.05$, two-sided t test). The difference was not significant for BW neurons ($p > 0.05$, t test). The suppression for NW-burst neurons was significant as compared to the NW-nonburst and BW neurons ($p < 0.001$ and $p < 0.01$, permutation test). Error bars and shadings in (A), (B), (C), and (E) indicate SEs of the mean.

the spike train with a Gaussian kernel (the spike-density function; see STAR Methods). This spike-density function was computed only for the preferred stimulus orientation. We then fitted a sinusoid to this spike-density function and computed a modulation measure as $M = (F_1 - F_0)/(F_0 + F_1)$ (see STAR Methods). Here, F_1 is the amplitude of the sinusoid (corrected for estimation bias) and F_0 is the mean elevation of firing above baseline (see STAR Methods). Values of M below and above zero indicate complex-cell and simple-cell modulation, respectively. In line with previous work, we observed a bimodal distribution of modulation values (Hartigan's dip test, $p < 0.05$). Most neurons had complex receptive-field properties, which is consistent with the placement of our electrodes in superficial layers (Figure 4C; $M < 0$ for 76% of NW-burst neurons; NW-nonburst, 85%; BW, 70%). The discharge rates of BW neurons were more strongly modulated by the

phase of the drifting gratings than the rates of NW-nonburst neurons (Figure 4C). NW-burst neurons mainly had complex RF properties and did not significantly differ from NW-nonburst and BW neurons (Figure 4C). In sum, neurons mainly had complex RFs, and the RFs of NW-nonburst neurons tended to be more like the complex type.

We found that NW-burst neurons were more selective for stimulus orientation than the other cell classes. We had expected the opposite finding because of their high spontaneous discharge rates. One explanation could be that these neurons receive broadly tuned and strong inhibitory inputs restricted to the period of visual stimulation (Shapley et al., 2003; Isaacson and Scanziani, 2011). This would decrease their excitability and thereby sharpen their orientation tuning. To examine this, we compared the neurons' discharge rates between the stimulus and pre-stimulus periods. We observed that some of

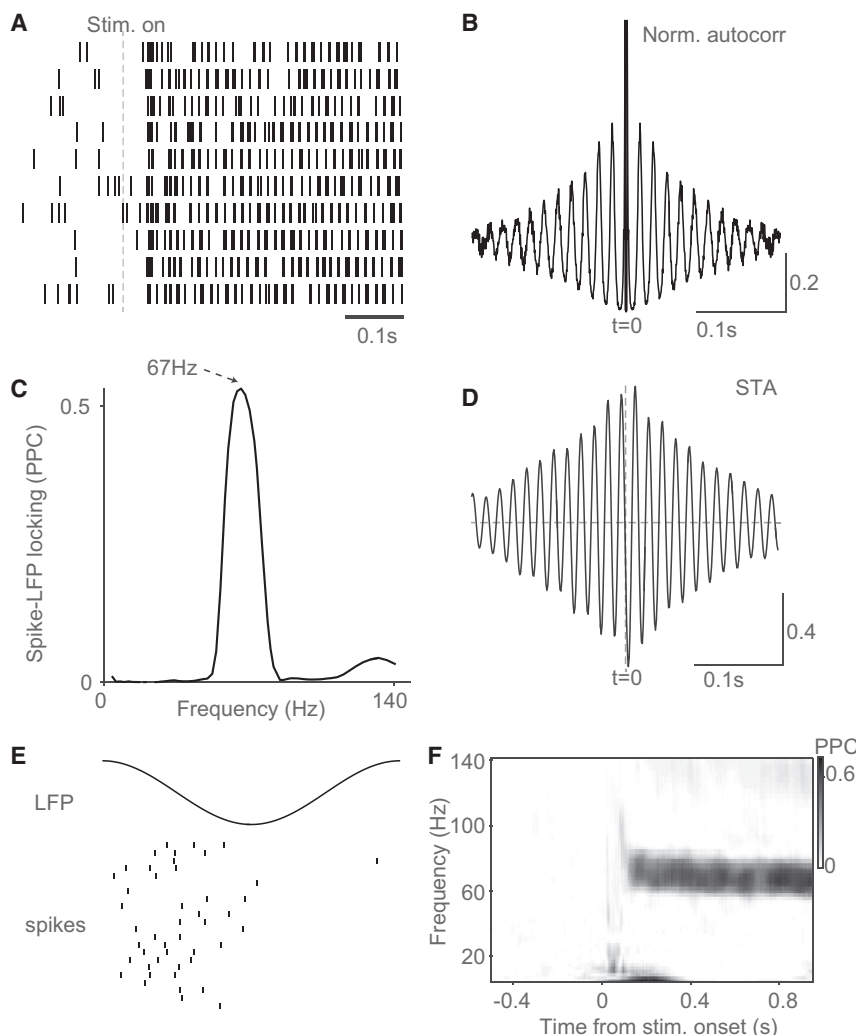


Figure 5. Spike-LFP Gamma-Phase Locking for an Example NW-Burst Neuron (Same Neuron as in Figure 2B)

(A) Raster plot of spikes recorded in response to a drifting grating with the neuron's preferred stimulus-direction. Shown are the first 10 trials.

(B) Normalized (between 0 and 1) autocorrelogram during the visual stimulation period (>200 ms after stimulus onset). The autocorrelogram had oscillatory side lobes at a period of the gamma cycle (~15 ms), which indicates gamma-rhythmic firing.

(C) Spectrum of spike-LFP gamma-phase locking as a function of frequency (Hz). Spike-LFP phase locking was estimated with the pairwise phase consistency (PPC; see STAR Methods).

(D) Spike-triggered average (STA) of the LFP as a function of time (s). Before computing the STA, we Z-scored the LFP signals. The STA has oscillatory side lobes at the period of a gamma cycle, similar to the autocorrelogram.

(E) Raster plot of spikes as a function of gamma phase. Each row represents a different gamma cycle. We show a selection of gamma cycles that had a duration of 15 ms and that were detected during the trials in which the preferred stimulus direction was presented. Spikes were clustered at the falling phase of the LFP gamma cycle.

(F) Spike-LFP gamma-phase locking (PPC) as a function of frequency (Hz) and time (s). The neuron showed gamma-phase locking shortly after the onset of the visual stimulus. This gamma locking was sustained throughout the stimulus period.

the NW-burst neurons were highly suppressed at their non-preferred stimulus orientation (Figure 4D). To study this phenomenon at the population level, we determined the mean discharge rates for each stimulus orientation separately. We found that the discharge rates of NW-burst neurons were suppressed below baseline levels for non-preferred orientations (Figures 4D and 4E). This pattern was not observed for NW-nonburst and BW neurons (Figure 4E). Thus, NW-burst neurons encoded stimulus orientation not only with an increase but also with a decrease in firing relative to the pre-stimulus period. This finding is consistent with the study of Shapley et al. (2003), who found that some V1 neurons show suppression at non-preferred stimulus orientations. Together, this indicates that NW-burst neurons receive a strong inhibitory drive during the visual-stimulation period, which can sharpen the tuning of these neurons (Shapley et al., 2003).

Differences in Rhythmic Firing

The way that V1 neurons transmit stimulus information via horizontal and feedforward connections likely depends on the syn-

chronization of their responses (Fries, 2015; König et al., 1996; Salinas and Sejnowski, 2000). Many visual stimuli induce prominent 30- to 80-Hz gamma-oscillations in primate V1 (Fries, 2009; Vinck and Bosman, 2016; Lima et al., 2010). However, the contributions of different

neuron types to gamma-synchronization in primate V1 remain largely unknown.

To investigate this, we compared the strength of spike-LFP phase locking among the three neuron types. For each spike, we determined its phase relative to the LFP recorded from the other electrodes (see STAR Methods). After computing the spike-LFP phases, we estimated phase locking using the pairwise phase consistency (PPC) measure (Vinck et al., 2012). The PPC is not affected by mean discharge rates and history effects like bursting (see STAR Methods; Vinck et al., 2012). Thus, it can be used to compare neuron types with different levels of discharge rates and burst propensity. Gamma-phase locking is illustrated for an example NW-burst neuron in Figure 5. We found that all three neuron types were phase locked to LFP gamma oscillations within a narrow frequency range (Figures 6A–6C and S7A). Yet, NW-burst neurons showed much stronger gamma-phase locking than BW and NW-nonburst neurons (~2.5-fold difference; $p < 0.05$, permutation test). This pattern was consistent across the two monkeys (Figures 6A, S7A, and S7B). This is consistent with the presence of rhythmic side

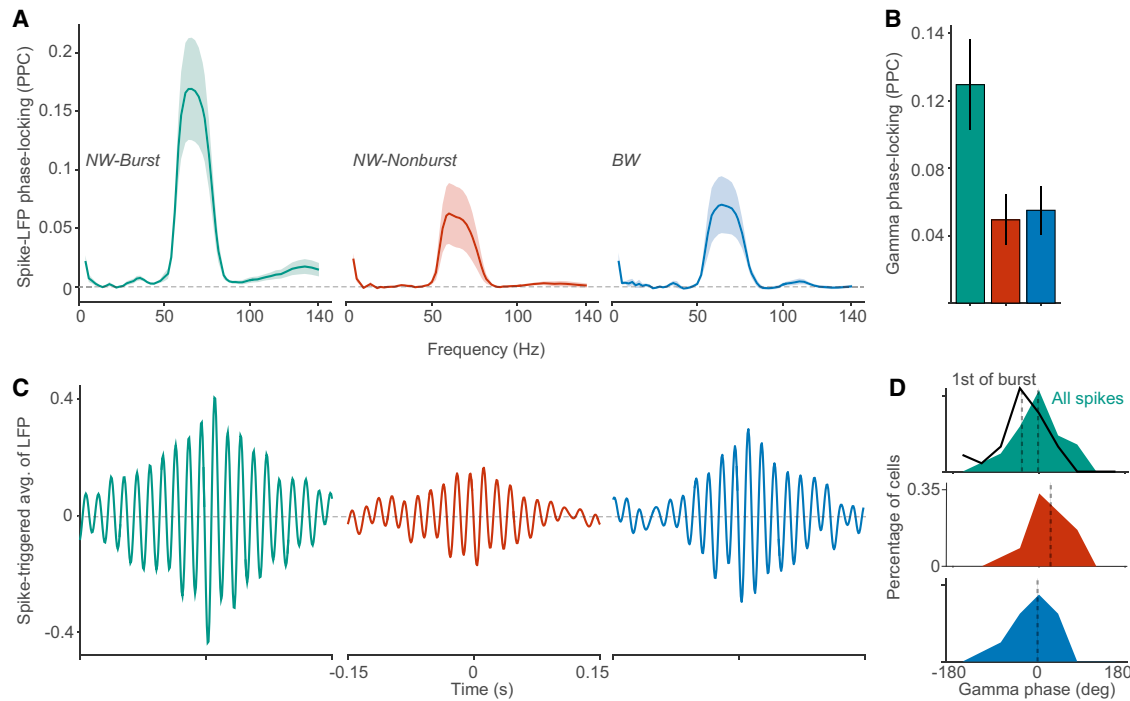


Figure 6. NW-Burst Neurons Were More Gamma-Phase Locked than NW-Nonburst and BW Neurons

(A) Mean spike-LFP phase-locking (PPC) values as a function of frequency (Hz) for monkey J. We computed the spike-LFP phases using a short-term Fourier transform with nine cycles per frequency and a Hann taper (see STAR Methods). For monkey L, see Figure S7A.

(B) Mean gamma-phase locking (PPC) across all recorded neurons from both macaques. In this case, we computed the spike-LFP phases by determining the peaks and troughs of the band-pass filtered LFP signals (see STAR Methods). NW-burst neurons had higher gamma-phase locking than NW-nonburst and BW neurons (2.62 and 2.35 times stronger; both comparisons $p < 0.01$, permutation test; see STAR Methods). BW and NW-nonburst neurons were not significantly different ($p > 0.05$).

(C) Bottom: mean spike-triggered average (STA) of the LFP as a function of time around the spike. We computed the mean STAs by averaging across neurons. Before computing the STA, we Z-scored the LFP signals. Note that the STA is biased as a function of the spike count, such that lower spike counts yield STAs with a smaller amplitude. The STAs exhibit oscillatory side lobes, whose amplitude decays slowly over time. This is consistent with the narrow-band character of spike-LFP phase locking.

(D) Distribution of preferred gamma phases across neurons. Shown is the difference between the preferred gamma phases of the single units and the same-site MUAs (see STAR Methods). The spikes of NW-nonburst neurons were significantly delayed relative to the same-site MUA spikes (95% confidence intervals, 11.7–84.6 degrees; difference compared with BW and NW-burst neurons, $p < 0.05$, permutation test). The black line shown together with the phase distribution of NW-burst neurons (turquoise) represents the phase distribution of the first spikes in the burst, which was significantly advanced relative to the distribution of all spike phases (turquoise, filled).

Error bars and shadings in (A) and (B) indicate SEs of the mean.

lobes in the autocorrelogram of NW-burst neurons (Figure 2D). Note that a small subset of NW-nonburst neurons exhibited rhythmic side lobes in the autocorrelogram (Figure 2C). In sum, we find that the class of NW-burst neurons are strongly gamma synchronized compared to other cell classes.

Gamma oscillations are often studied in the later part of the stimulus period, which avoids the non-stationary, transient response that occurs shortly after stimulus onset. The way in which we computed the spike-LFP phases allowed us to study gamma-phase locking in an earlier part of the stimulus period (100–250 ms after stimulus onset; see STAR Methods). Also in this early phase of the stimulus period, NW-burst neurons were more gamma-phase locked than NW-nonburst and BW neurons (Figure S7C). We observed similar levels of phase locking in the early and late phase of the stimulus period (>200 ms after stimulus onset). Hence, gamma-phase locking may play a functional role in “early vision.”

Many factors can influence gamma-phase locking, such as the laminar position of the electrode and the state of the animal (van Kerkoerle et al., 2014; McGinley et al., 2015b; Herculano-Houzel et al., 1999; Livingstone, 1996; Vinck et al., 2015; Senzai et al., 2019; McGinley et al., 2015a; Zagha et al., 2013; Xing et al., 2012; Herculano-Houzel et al., 1999; Gray et al., 1992; Besserve et al., 2015). These factors may have contributed to the observed differences between neuron types. To investigate this, we used a similar method as in Vinck et al. (2013a): for each single unit, we constructed a “same-site multi-unit-activity (MUA)” signal. This signal contained all the remaining spikes that were recorded from an electrode, after excluding the activity of the isolated single units. For each same-site MUA, we computed the phase locking of MUA spikes to LFP oscillations (PPC). This allowed us to make a comparison between same-site MUAs corresponding to NW-burst, NW-nonburst, and BW neurons. We did not observe a significant difference in phase locking among the

same-site MUAs of NW-burst, NW-nonburst, and BW neurons (all comparisons $p > 0.05$, permutation test). Moreover, NW-burst neurons had much higher gamma-phase locking than the same-site MUA (Figure S7B). This was not the case for NW-nonburst and BW neurons (Figure S7B). These results suggest that other factors like electrode position and behavioral state did not explain the differences in gamma locking between neuron types.

Discharge rates and burst propensity could also have influenced gamma-phase locking. Note that the PPC measure removes biases due to spike count and/or history effects like bursting (Vinck et al., 2012). Nevertheless, we wanted to examine whether burst propensity and discharge rates correlate with phase locking. For each neuron type, we correlated the pre-stimulus discharge rates with the gamma-phase locking during the visual stimulation period. We found no significant correlation for any of the three neuron types (NW-burst, $p = -0.2976$; NW-nonburst, -0.1174 ; BW, 0.0220 ; $p > 0.05$ for all neuron types). Likewise, burst propensity (measured during the stimulus period) was not significantly correlated with gamma-phase locking (NW-burst, $p = -0.1202$; BW, -0.0098 ; $p > 0.05$; note that NW-nonburst neurons lacked the necessary bursts for this analysis). In fact, the high burst-propensity of NW-burst neurons may have decreased their phase locking. Suppose that a neuron fires in bursts, and that the first spike of a burst is always precisely timed to the onset of the gamma cycle. The other spikes of the burst would then occur at later gamma phases, thereby reducing phase locking. To investigate this possibility for NW-burst neurons, we detected all bursts and computed the gamma-phase locking for the set of spikes that came first in a burst. Indeed, we confirmed that the first spikes of the burst were (~ 2 -fold) more gamma-phase locked than all spikes together (Figure S7E). This means that the gamma-phase locking of NW-burst neurons was even more precise for the first spikes of their bursts.

Models of gamma oscillations make specific predictions about the relative timing of different neuron types within the gamma cycle (Buzsáki and Wang, 2012; Wang, 2010; Tiesinga and Sejnowski, 2009; Börgers and Kopell, 2005, 2008). We therefore asked whether the three different neuron types fired at similar phases of the gamma cycle or whether they fired in a specific sequence. Previous studies on gamma have found that fast-spiking interneurons fire with a short delay after E neurons, which is consistent with pyramidal interneuron network gamma (PING) models of gamma generation (Vinck et al., 2013a; Csicsvari et al., 2003; Hasenstaub et al., 2005). In PING models, a rise in excitatory-cell firing triggers an increase in inhibitory-cell firing at a short delay, leading to a subsequent decrease in the firing of excitatory cells (Buzsáki and Wang, 2012; Tiesinga and Sejnowski, 2009; Börgers and Kopell, 2005, 2008; Wang, 2010). Whether these dynamics can be observed in area V1 remains unknown. For each neuron, we determined the gamma phase at which its discharge rate reached a peak (the preferred gamma phase; see STAR Methods). A potential caveat in the analysis of spike-LFP phases is that there is substantial variability in the phase of firing across recording sites (Vinck et al., 2013a; Livingstone, 1996; van Kerkoerle et al., 2014). This is caused by many factors, especially

the stimulus drive and the laminar position of the unit or LFP (Livingstone, 1996; van Kerkoerle et al., 2014; Vinck et al., 2010a, 2013a). To remove this variability, we computed the preferred gamma phase for each of the same-site MUAs (see STAR Methods). We then computed the difference between the preferred gamma phases of the single unit and of its corresponding same-site MUA. The distributions of phase differences is shown in Figure 6D. We found that the firing of NW-nonburst neurons was delayed relative to the same-site MUA (Figure 6D). By contrast, the phase of NW-burst and BW neurons did not differ relative to the same-site MUA (Figure 6D). NW-nonburst neurons fired significantly later in the gamma cycle than NW-burst and BW neurons ($p < 0.05$, permutation test; see STAR Methods).

The analysis on firing phases above was performed by pooling the phases of all spikes together. However, NW-burst neurons have a high burst propensity, and the analysis presented in Figure S7E shows that the first spike of the burst is very precisely phase locked to the gamma cycle. The consequence may be that the spikes occurring later in the burst fall at a later gamma phase, which would shift the mean phase-of-firing to a later gamma phase. We therefore predicted that the first spike of the burst should be significantly advanced as compared to the mean phase of all spikes together and precedes the firing of NW-nonburst neurons by a larger degree. Indeed, the first spike of the burst of NW-burst neurons preceded the mean phase of all NW-burst spikes by 38.4° ($p < 0.05$, bootstrap test) and preceded NW-nonburst firing by 59.8° on average ($p < 0.05$, permutation test) (Figure 6D). Thus, the first spike of the burst fired by NW-burst neurons precedes (putative) interneuron activity by several milliseconds (Figure 6D). The early onset (Figure 6D) and precise timing of the first-of-the-burst spikes in the gamma cycle (Figure S7E) suggest that they could play an important role in the ignition of gamma oscillations through their effect on GABAergic interneurons. Together, these findings are consistent with the idea that NW-nonburst neurons correspond to fast-spiking inhibitory interneurons and fire with a short delay after E neurons.

Dependence of the Discharge Rate on the Gamma Phase

In the analysis of orientation tuning presented above, we observed that the firing of NW-burst neurons was suppressed for the non-preferred stimulus orientation (Figures 4D and 4E). This suggests that these neurons receive a very strong inhibitory drive during the visual stimulation period. We wondered whether a similar suppression occurs during the non-preferred LFP gamma phases of NW-burst neurons. The non-preferred gamma phase of a neuron is defined as the gamma phase at which its discharge rate reaches a minimum. We determined neuronal discharge rates as a function of the gamma phase as follows: We first binned the LFP gamma cycle in 40 nonoverlapping phase bins. We then determined the amount of time that the LFP spent in a given gamma-phase bin. This was equal to $T = \sum(T_i/40)$, where T_i is the duration of the i^{th} recorded gamma cycle. The discharge rate in the k^{th} phase bin then equaled N_k/T , where N_k is the number of recorded spikes in that phase bin. The discharge rate as a function of gamma phase for an example NW-burst neuron is shown in Figures 7A and 7B.

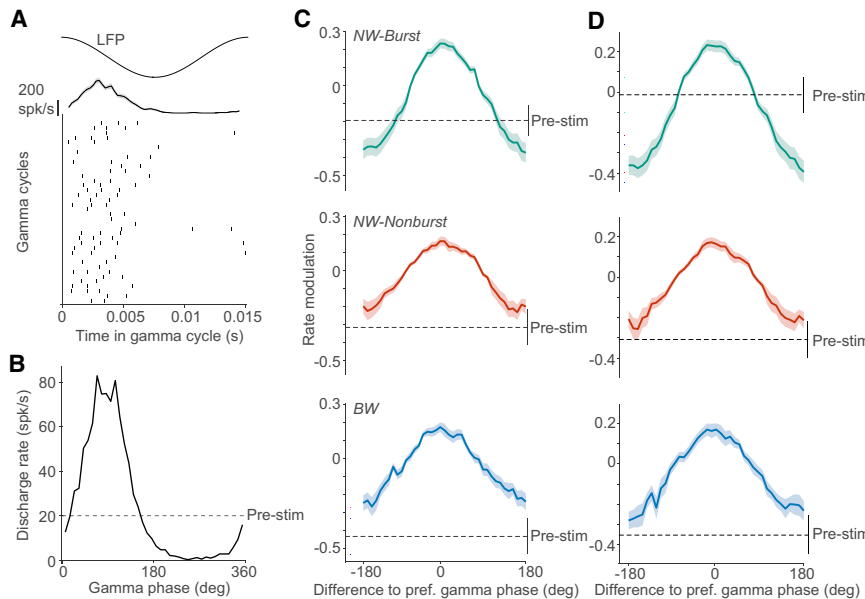


Figure 7. Discharge Rates of NW-Burst Neurons Were Suppressed at Their Non-preferred Gamma Phase

(A) Example NW-burst neuron (same neuron as in Figure 2B). Raster plot of spikes in the gamma cycle. Each row represents a different gamma cycle, aligned to the LFP peak. We show a selection of gamma cycles that had a duration of 15 ms and were detected during trials in which the preferred stimulus direction was presented. At the top, we show the instantaneous discharge rate as a function of the gamma phase.

(B) Mean discharge rate (spikes/s) as a function of the gamma phase (degrees) for the example neuron shown in (A). We computed the mean discharge rate by averaging across all stimulus trials. The dashed line represents the neuron's pre-stimulus discharge rate.

(C) Mean modulation of the discharge rate as a function of the gamma phase (degrees). For each neuron, we computed the preferred gamma phase. The x axis represents the phase relative to the preferred gamma phase (degrees). The modulation of the discharge rate was computed as $(a - b)/(a + b)$. Here, a is the discharge rate for either one of the 40 gamma phases or for the pre-stimulus period. The variable b represents the mean discharge rate across gamma phases. The shading in (C) and (D) indicate SEMs of the mean.

dashed lines indicate the mean for the pre-stimulus period. The vertical line on the right indicates ± 1 SEM for the pre-stimulus period. NW-burst neurons were significantly suppressed relative to baseline ($p < 0.05$, t test). The difference between NW-burst and NW-nonburst and BW neurons was significant ($p < 0.05$, permutation test; see STAR Methods).

(D) Similar to (C), but now computing the discharge rates in a different way. For each k^{th} gamma phase bin, we determined whether the last spike had occurred at least \bar{T} milliseconds before the gamma phase bin, where \bar{T} was the average period of the gamma cycle. We then counted the number of phase bins for which this was the case, and computed the total amount of time spent in that gamma phase bin, T . The discharge rate then equaled N_k/T , where N_k is the number of spikes in those gamma-phase bins (i.e., occurring after a pause of no firing for \bar{T} ms). NW-burst neurons were significantly suppressed relative to baseline ($p < 0.001$, t test). The difference between NW-burst and NW-nonburst and BW neurons was significant ($p < 0.001$).

Shadings in (C) and (D) indicate SEMs of the mean.

This neuron was virtually silent at its non-preferred gamma phase (Figure 7B). We found that on average, the discharge rates of NW-burst neurons were suppressed during non-preferred phases of the gamma cycle (Figure 7C). This suppression was not found in NW-nonburst and BW neurons (Figure 7C).

One possible explanation for the suppression of discharge rates during the non-preferred gamma phase is a strong inhibitory input drive arriving at that phase. An alternative explanation could be that NW-burst neurons are silent at their non-preferred gamma phases because they have already fired at an earlier phase. This could suppress firing at later gamma phases, if these phases occur during the neuronal refractory period. To distinguish between these two scenarios, we computed discharge rates in an alternative way: for each k^{th} gamma phase bin, we determined whether the last spike had occurred at least \bar{T} milliseconds before the gamma phase bin, where \bar{T} was the average period of the gamma cycle. We then counted the number of phase bins for which this was the case and computed the total amount of time spent in that gamma phase bin, T . The discharge rate then equaled N_k/T , where N_k is the number of spikes in those gamma phase bins (i.e., occurring after a pause of no firing for \bar{T} ms). We found that the suppression at the non-preferred gamma phase for NW-burst neurons was even more pronounced when the discharge rates were calculated in this

way (Figure 7D). Hence, firing suppression at the non-preferred gamma phase was not due to the neuronal refractory period.

In sum, a unique feature of NW-burst neurons is that their firing is decreased below pre-stimulus levels during the non-preferred gamma phase. This is a surprising finding, considering that visual stimuli should increase the excitatory drive to NW-burst neurons. It thus suggests that these neurons receive a strong inhibitory input drive at the non-preferred gamma phase. Notably, in Figures 4D and 4E, we showed a similar suppression of NW-burst neurons for non-preferred stimulus orientations.

Relationship between Gamma and Orientation Tuning

We observed differences in both orientation selectivity and gamma synchronization between neuron types. In particular, we found that NW-burst neurons have both high orientation selectivity and gamma-phase locking as compared to other neuron types. Previous work has suggested a close relationship between these two aspects of V1 activity (Friedman-Hill et al., 2000; Vinck et al., 2010a; Womelsdorf et al., 2012; Maldonado et al., 2000). We previously reported a positive correlation between gamma-phase locking and orientation selectivity across neurons (Womelsdorf et al., 2012). It is likely that this positive correlation was partly due to the strong phase locking and orientation selectivity of NW-burst neurons. We therefore revisited

this analysis and examined the correlations for the three neuron classes separately. NW-burst neurons showed a highly positive correlation between orientation selectivity (OSI) and gamma-phase locking values (*Figures 8A* and *8B*; $p < 0.001$, bootstrap test). This correlation was weaker and not significant in the other two neuron types (*Figures 8A* and *8B*; $p > 0.05$, bootstrap test; NW-burst versus BW and NW-nonburst, $p < 0.05$, permutation test). NW-burst neurons also showed a negative correlation between gamma-phase locking and the extent to which their firing was modulated by the phase of the grating (i.e., simple versus complex) ($R = -0.27$, $p < 0.05$, bootstrap test). Thus, NW-burst neurons with more complex RFs and stronger orientation tuning were also more gamma-phase locked.

Previous experimental and computational work has suggested that gamma oscillations depend on stimulus drive (Ray and Maunsell, 2010; Peter et al., 2019; Bartos et al., 2007; Gray et al., 1990; Gray and Viana Di Prisco, 1997; Roberts et al., 2013; Jia et al., 2011, 2013; Chalk et al., 2010). For example, gamma amplitude increases with luminance contrast (Henrie and Shapley, 2005; Ray and Maunsell, 2010; Gray and Viana Di Prisco, 1997; Roberts et al., 2013) and it can be abolished by stimulus adaptation (Peter et al., 2019). What explains this drive dependence? It could be that sufficient drive to the entire neuronal population is required for the emergence of gamma synchronization. An alternative possibility is that a single neuron can only entrain to gamma oscillations when its membrane potential is sufficiently depolarized. Because luminance contrast modulates the firing of most neurons in V1, its manipulation cannot be used to distinguish between these two scenarios. However, when we present a grating with a specific stimulus orientation, some neurons will be strongly driven, and other neurons in the same hypercolumn will be suppressed. For example, the NW-burst neuron shown in *Figure 8C* was strongly suppressed during the presentation of its non-preferred stimulus orientations (*Figure 4B*). Yet, it still showed gamma-phase locking for non-preferred orientations (*Figure 8C*), suggesting that a given neuron can be strongly gamma locked even if it is not strongly driven.

To investigate this at the population level, we used two approaches. In the first approach, we compared the gamma-phase locking between a neuron's best (i.e., preferred) stimulus orientation and its three worst (i.e., non-preferred) orientations (*Figure 8D*). The best orientation was defined as the orientation at which its discharge rate was maximum. Note that we pooled the three worst orientations to obtain a sufficient amount of spikes to reliably estimate spike-LFP locking values. Surprisingly, we found that for all three neuron types, gamma-phase locking was not higher for the preferred stimulus orientations than the non-preferred stimulus orientations (t test, $p > 0.05$; *Figure 8D*). However, it could be that there was some stimulus drive for the non-preferred stimulus orientations, which could have resulted in gamma-phase locking. We therefore selected the NW-burst neurons whose discharge rates were suppressed below baseline for their three worst stimulus orientations. Also for these neurons, we found that gamma-phase locking did not significantly differ between non-preferred and preferred stimulus orientations (t test, $p > 0.05$; *Figure 8D*). Thus, gamma-phase locking was largely independent of stimulus orientation and re-

mained strong even when discharge rates were suppressed below baseline levels. This suggests that a neuron's gamma-phase locking depends on sufficient drive to the entire network, but not on the excitatory drive to that individual neuron.

However, this analysis may have been insensitive, because we ignored a subset of orientations. In the second approach, we predicted the PPC values from the discharge rate across all the 16 stimulus directions (*Figure 8E*). For each neuron, we computed the discharge rates for the 16 different stimuli separately. The firing rates were normalized by dividing by the maximum discharge rate. Thus, normalized discharge rates were bounded by 0 (a discharge rate of zero) and 1 (the maximum discharge rate). We then predicted the 16 gamma-phase locking values from the 16 normalized discharge rates (see **STAR Methods**). The slope of the regression models indicated the change in PPC as the normalized discharge rate increased from 0 to 1. The intercept indicated the level of phase locking that would be expected if the discharge rates converged to zero. We found that gamma-phase locking was positively related to discharge rates for all three neuron types (t test, $p < 0.05$; *Figure 8E*). However, the regression intercepts were significantly higher than zero for NW-burst neurons, but not for BW and NW-nonburst neurons (t test, $p < 0.001$; *Figure 8D*). This indicates that NW-burst neurons exhibited strong gamma-phase locking even when their discharge rates approached zero (*Figure 8E*). This result is consistent with the direct comparison of preferred and non-preferred orientations shown in *Figure 8D*. In addition, this analysis shows that gamma-phase locking increased as a function of stimulus-driven discharge rates.

DISCUSSION

Summary

The contributions of distinct neuron types to synchronization and stimulus selectivity in primate V1 remain largely undetermined. We recorded spikes and LFPs from awake macaque V1 and analyzed AP waveforms to distinguish between NW and BW neurons. NW and BW APs are commonly used to identify fast-spiking interneurons and excitatory cells, respectively. Surprisingly, most neurons in macaque V1 had an NW AP. By analyzing firing statistics, we showed that NW neurons form two separate clusters. NW-burst neurons had early peaks in the autocorrelogram and a high burst propensity. Conversely, NW-nonburst neurons had late peaks in the autocorrelogram and a low burst propensity. Similar firing patterns were observed in a New World capuchin monkey. Comparisons among NW-burst, NW-nonburst, and BW neurons revealed major differences in firing properties, visual selectivity, and oscillatory synchronization. NW-burst neurons were most strongly phase locked to 30- to 80-Hz gamma oscillations and were most stimulus selective. Furthermore, we found signatures of strong rhythmic inhibition in NW-burst neurons, suggesting that they interact with GABAergic interneurons to generate the V1 gamma rhythm.

Classification of Neuron Types

We distinguished three neuron types based on AP waveform and firing properties. One class of neurons had BWs. Previous

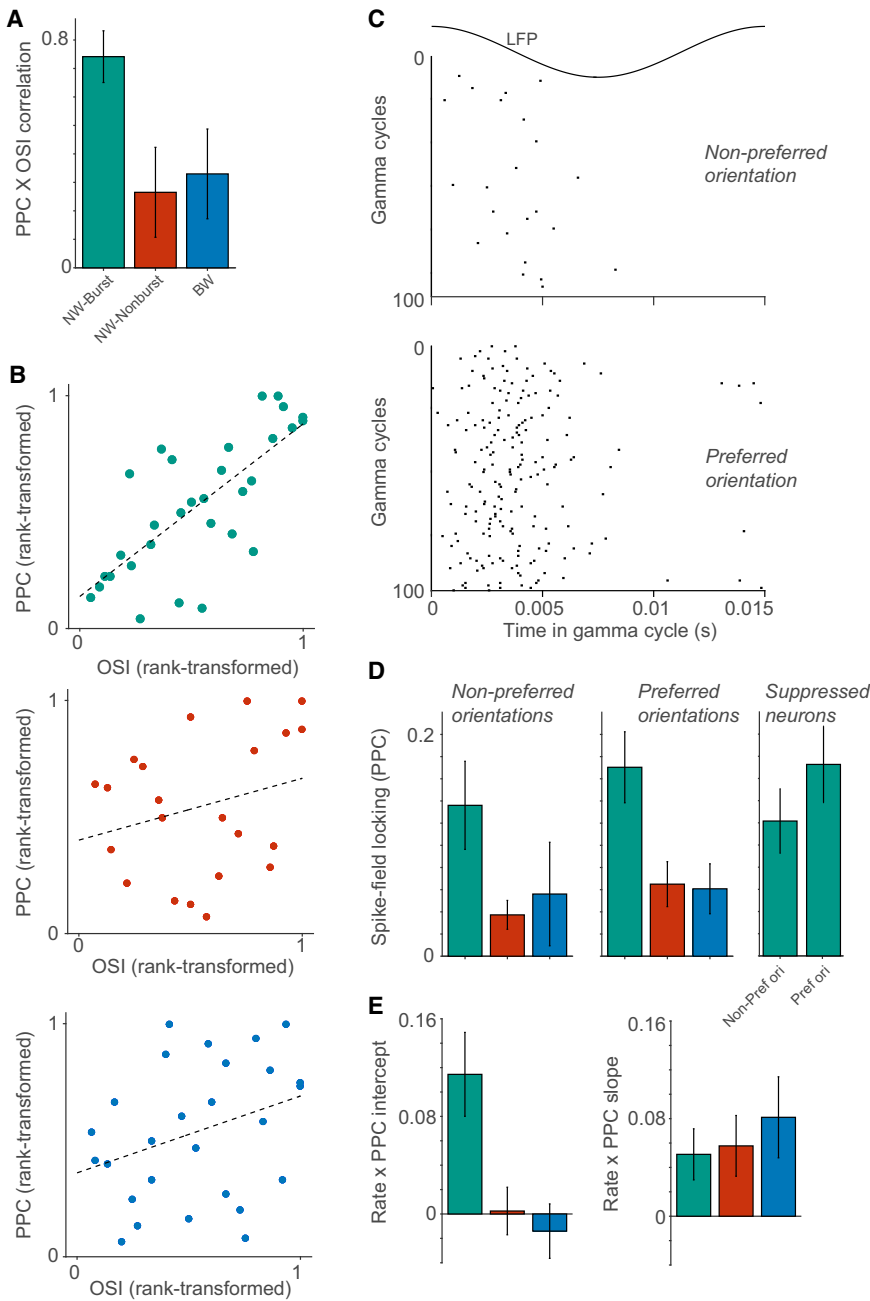


Figure 8. The Gamma-Phase Locking of NW-Burst Neurons Was Strongly Correlated with Their Orientation Selectivity

NW-burst neurons were also gamma-phase locked for non-preferred stimulus orientations.

(A) Rank correlation between orientation-selectivity index (OSI) and spike-LFP phase locking (PPC). We first rank transformed the OSI and PPC values and normalized the rank scores between 0 and 1. We then pooled the normalized ranks across the two monkeys and computed the Pearson's correlation coefficient. Because of the rank transformation, this coefficient is comparable to the Spearman's rho correlation. We computed the SEMs by bootstrapping over neurons. Correlations were significantly higher for NW-burst than NW-nonburst and BW neurons ($p < 0.05$, permutation test).

(B) Correlation between OSI and PPC for NW-burst neurons (top), NW-nonburst neurons (middle), and BW neurons (bottom). We show the normalized ranks of the OSI (x axis) and PPC (y axis).

(C) Raster plot of spikes as a function of gamma phase for an example NW-burst neuron (same neuron as in Figure 2B). Each row represents a different gamma cycle, aligned to the LFP peak. We show a selection of gamma cycles that had a duration of 15 ms. Top and bottom: gamma cycles that were detected during trials in which a non-preferred (top; fourth orientation from the top in Figure 4D) or preferred (bottom) stimulus orientation was presented.

(D) Left: spike-LFP phase locking (PPC) for the three stimulus orientation at which the neuron discharge rates were the lowest. For (D), we only included neurons that were significantly orientation tuned. Middle: PPC for the stimulus orientation at which the neuron discharge rates were the highest. Right: same analysis, but now for NW-burst neurons whose firing rates were suppressed relative to baseline for the three non-preferred stimulus orientations. There were no significant differences between preferred and non-preferred stimulus orientations for all comparisons ($p > 0.05$).

(E) Left: mean intercept for the regression of spike-LFP gamma-phase locking (PPC) onto discharge rate. For each neuron, we computed the discharge rate and PPC for each stimulus direction separately. We normalized the discharge rates by dividing by the maximum discharge rate. We then predicted the PPC values from the

discharge rates. The intercept estimates the PPC as the normalized discharge rate converges to 0. Right: mean slope for the regression of PPC onto discharge rate.

Error bars in (A), (D), and (E) indicate SEMs of the mean.

studies have identified these as excitatory (Rudy et al., 2011; Gentet et al., 2012; Nowak et al., 2003; Vinck et al., 2016; Senzai et al., 2019; Miri et al., 2018; Perrenoud et al., 2016; Hasenstaub et al., 2005). Like previous studies, we found that BW neurons had low spontaneous discharge rates and that a subset of BW neurons exhibited burst firing (Vinck et al., 2016; Senzai et al., 2019; Barthó et al., 2004; Nowak et al., 2003; Csicsvari et al., 1999, 2003).

The firing properties of NW-nonburst neurons were comparable to those of fast-spiking inhibitory interneurons: (1) NW-nonburst neurons had late peaks in the autocorrelogram, which indicates a low burst propensity. Similar firing characteristics have been described for fast-spiking interneurons in other cortical areas (Nowak et al., 2003; Csicsvari et al., 2003; Vinck et al., 2013a, 2016; Senzai et al., 2019; Perrenoud et al., 2016; Csicsvari et al., 1999), and we observed these in mouse L2/3

NW neurons (see Figure S4). (2) They had high discharge rates, which is a common characteristic of fast-spiking interneurons (Csicsvari et al., 2003; Nowak et al., 2003; Senzai et al., 2019; Vinck et al., 2013a; Perrenoud et al., 2016; see Figure S4). (3) They had low stimulus selectivity, in line with previous studies (Kerlin et al., 2010; Nowak et al., 2008; Perrenoud et al., 2016). (4) They fired with a short time delay (~2 ms) after neurons in their vicinity (Figure 6D). This is consistent with many models of excitatory-inhibitory interactions, such as PING models (Buzsáki and Wang, 2012; Wang, 2010) and previous experimental characterizations (Csicsvari et al., 2003; Hasenstaub et al., 2005; Vinck et al., 2013a).

NW-burst neurons had early peaks in the autocorrelogram and a high burst propensity. Previously, Gray and McCormick (1996) identified a subset of neurons in area V1 of the anesthetized cat that had NW APs and responded to intracellular current depolarization with rhythmic bursts. These neurons are presumably excitatory, considering that they had spiny pyramidal morphology and an axon extending into the white matter. Neurons with similar responses to intracellular currents have also been observed in motor and suprasylvian association areas of the cat (Steriade et al., 1998, 2001). Gray and McCormick (1996) named these neurons “chattering cells,” and they resemble the NW-burst neurons described here in several respects: (1) NW-burst neurons fired in patterns of high-frequency bursts with an intra-burst frequency up to 400–500 Hz, matching the intra-burst frequency of chattering neurons (Nowak et al., 2003; Cardin et al., 2005; Gray and McCormick, 1996; Steriade et al., 1998). Note that another class of bursting E neurons, intrinsic bursting neurons, has BWs and a lower intra-burst frequency (Nowak et al., 2003). (2) NW-burst neurons had much higher spontaneous discharge rates than BW neurons, consistent with the finding that chattering neurons show little adaptation to depolarizing current injections (Gray and McCormick, 1996; Nowak et al., 2003). By contrast, the responses of BW neurons adapt strongly over time, and this leads to cycle skipping (Nowak et al., 2003; Gray and McCormick, 1996). Note that high spontaneous discharge rates (found in NW-burst neurons) are in general not a simple consequence of burst firing, because bursting BW neurons have lower spontaneous discharge rates than non-bursting BW neurons (Vinck et al., 2015, 2016; Senzai et al., 2019). Finally, we found that NW-burst neurons were strongly stimulus selective, whereas NW-nonburst neurons were weakly stimulus selective. This would be expected if NW-burst and NW-nonburst neurons correspond to E and I neurons, respectively (Kerlin et al., 2010; Nowak et al., 2008; Perrenoud et al., 2016).

While there are several similarities between NW-burst neurons and chattering cells, further research is required to clarify their precise relation. The majority of chattering neurons in L2-L4 of the anesthetized cat V1 have simple RFs (Cardin et al., 2005; Nowak et al., 2003; Gray and McCormick, 1996). By contrast, we found that in awake monkey V1, the RFs of NW-burst neurons were predominantly complex and that NW-burst neurons with more complex RFs were more gamma rhythmic. This finding is consistent with the study of Gray et al. (1990), who found that in lightly anesthetized cats, oscillatory responses were much more frequent in neurons with complex RFs than in neurons with

simple RFs. Future work is needed to examine more precisely the dependence of RF properties on anesthesia and further explore potential differences between cats and primates.

Our data also suggest that it is unlikely that the sample of NW-burst neurons includes a substantial fraction of L4 spiny-stellate neurons, which have NW spikes (Gur et al., 1999). Whereas spiny-stellate cells are located in L4, our recordings were biased toward superficial layers (L2/3). This is consistent with the presence of strong gamma synchronization in our dataset, given that gamma is strong in superficial layers and quite weak in L4 (Livingstone, 1996; Xing et al., 2012; Buffalo et al., 2011; Gray et al., 1990). In addition, our recorded neurons mainly had complex RFs, which are typical for layers 2/3, but not for layer 4 (Martinez and Alonso, 2003). By contrast, the majority of spiny stellate neurons have simple RF properties (Martinez and Alonso, 2003).

What Explains the Prevalence of NW and NW-Burst Neurons in Monkey V1?

Compared to monkey V1, we found that the fraction of NW neurons was much lower in L2/3 and L4 of mouse V1, and we did not observe a distinct class of NW-burst neurons in mouse V1. In macaque V4 and PFC (prefrontal cortex), the percentage of NW neurons is also much lower than what we found in monkey V1. (Vinck et al., 2013a; Mitchell et al., 2007; Ardid et al., 2015). Although intracellular recordings in cat V1 have identified a subset of E (“chattering”) neurons with NWs (Gray and McCormick, 1996; Nowak et al., 2003), their prevalence (i.e., percentage) cannot be easily assessed given the type of recordings and small sample sizes. We were surprised that such a large fraction of macaque V1 neurons had firing properties similar to the ones of chattering neurons. It remains to be investigated which factors account for the high prevalence of NW and NW-burst neurons in monkey V1. Several factors could play a role. (1) Behavioral state: it is unlikely that the high prevalence of NW-burst neurons is due to the specific behavioral task or visual stimulation, because NW-burst neurons also had a high burst propensity in the pre-stimulus period (Figures 3 and S5). Nonetheless, it is possible that NW-burst neurons may cease to fire burst during periods of low arousal (e.g., anesthesia or slow-wave sleep), for example due to an influence of acetylcholine on burst-firing (Wang, 1999). (2) Recording techniques: in electrophysiological recordings there may exist a bias toward recording from high-firing rate neurons. This bias can be due to electrode positioning and spike-sorting procedures and should be stronger for independently movable, sharp electrodes (used for macaque V1) than for high-density, laminar silicon probes (used for mouse V1). Thus, we may have overestimated the fractions of NW neurons in macaque V1, because these neurons had, on average, higher firing rates than BW neurons. To assess whether recording biases due to firing rate differences may have affected the percentage of NW neurons, we iteratively removed NW neurons with high firing rates until the sample-mean matched the mean rate of BW neurons. We found that the sample of NW neurons with the same mean rate as BW neurons still represented 61% of the total number of neurons (or 65% of the original sample of NW neurons), consistent with the substantial overlap in the firing rate distributions of NW and BW neurons (Figure 3B). This

suggests that possible sampling biases due to firing rate would have had only a small effect on the percentage of NW neurons. A comparison with the literature also suggests that the large fraction of NW neurons in macaque V1 is not due to sampling bias. First, one expects less sampling bias with silicon probes, which were used for the mouse V1 recordings, where the percentage of NW neurons was much smaller. However, recordings with silicon probes do not yield, in general, substantially lower percentages of NW neurons in primary sensory regions of the mouse (this study, 9.2%; [Senzai et al., 2019](#), 18.9%; [Barthó et al., 2004](#), 8.2%) as compared to studies using independently movable electrodes ([Batista-Brito et al., 2017](#), 8.9%; [Vinck et al., 2016](#), 10.3%; [Vinck et al., 2015](#), 17.8%). Second, previous studies that find substantially smaller percentages of NW neurons in other primate cortical areas (e.g., 18.7% in primate PFC; [Ardid et al., 2015](#)) were also based on recordings using sharp, independently movable electrodes ([Vinck et al., 2013a](#); [Ardid et al., 2015](#); [Mitchell et al., 2007](#)). These analyses and considerations suggest that it is unlikely that the large fraction of NW neurons in macaque V1 is due to sampling bias. (3) Expression of specific channels in E neurons: differences in the proportions of electrophysiological classes between areas and species may reflect the expression of specific channels in E neurons. For example, Kv3 voltage-gated potassium channels are expressed in many E neurons in macaque V1, but not in rodent V1 ([Constantinople et al., 2009](#)). In general, single-cell transcriptional analyses have suggested that the properties of E neurons may vary greatly across cortical areas, in contrast to GABAergic interneurons ([Tasic et al., 2018](#)). Transcriptomics analyses have suggested that in primate neocortex, area V1 has a highly distinctive gene-expression pattern compared to other cortical regions, both in L4 and other layers ([Bernard et al., 2012](#)). Moreover, this unique V1 gene-expression pattern is not observed in mice but is comparable between macaque and human ([Bernard et al., 2012](#)). Future studies should compare single-cell transcriptional data between different visual regions of the primate, and between species, in order to examine this at a single-cell resolution. (4) Differences in anatomical organization: it is possible that NW-burst neurons are a common feature across (many or all) neocortical areas and species but that they are overrepresented in macaque V1 due to differences in anatomical organization. In particular, differences in the lamination of the cortex could be an important factor, considering that electrophysiological properties of neurons vary substantially across neocortical layers ([Senzai et al., 2019](#)). Monkey V1 differs from primary sensory areas of the mouse in several respects: in primates, L2-L4 are developed prominently and comprise ~70% but only comprise ~50% of the primary sensory areas in mice. Related to this, L4 in primate V1 is commonly subdivided into four sub-layers, whereas L4 in mouse V1 is relatively thin and not divided into sub-layers. Within these L4 sub-layers, there is a sharp transition between L4C, the dominant pathway for thalamocortical projections, and the upper layers (based on neuronal nuclei [NeuN] and VGLUT2 staining) ([Balaram and Kaas, 2014](#)). Whereas L4C may be considered as the homolog of L4 in the mouse, there is a gradual transition between L4B, L4A, and L3 ([Balaram and Kaas, 2014](#)). In fact, the latter three sub-layers are considered part of L3 (L3C and L3B β) in Hässler's nomenclature.

(Hässler, 1966) and may in fact derive from a common L3 ([Balaram and Kaas, 2014](#)). Thus, L3 and the L3/4 transition zone (i.e., L4B and L4A in Brodmann's nomenclature) are highly developed in monkey V1, and it is possible that this is related to the high prevalence of NW-burst neurons. Consistent with this notion, [Nowak et al. \(2003\)](#) found that seven out of nine recorded chattering neurons in cat (which all had spiny pyramidal morphology) were confined to the lower half of L2/3 (with one out of nine cells located in L4). Future studies in primates should follow a similar approach as in mice by combining high-density laminar recordings with histological analysis ([Senzai et al., 2019](#)), in order to further investigate the relationship between electrophysiological cell classes and cortical lamination patterns.

Mechanistic and Functional Implications

Gamma oscillations in the 40- to 90-Hz range are thought to depend on interactions between E neurons and fast-spiking interneurons. Fast-spiking interneurons likely play a central role in the generation of gamma, because they exhibit gamma resonance, respond to excitatory input with high temporal precision, and can entrain E neurons through divergent projections to their peri-somatic compartments ([Jouhanneau et al., 2018](#); [Pike et al., 2000](#); [Wang, 2010](#); [Buzsáki and Wang, 2012](#); [Cardin et al., 2009](#); [Hasenstaub et al., 2005](#); [Chen et al., 2017](#); [Kopell et al., 2000](#); [Perrenoud et al., 2016](#); [Vinck et al., 2013b](#); [Börgers and Kopell, 2008](#), 2005; [Lytton and Sejnowski, 1991](#); [Jadi and Sejnowski, 2014](#); [Whittington et al., 1995](#); [Sohal et al., 2009](#); [Wang and Buzsáki, 1996](#); [Womelsdorf et al., 2014](#); [Bush and Sejnowski, 1996](#); [Whittington et al., 2000, 2011](#); [Bartos et al., 2007](#)) Inter-areal gamma-coherence also likely depends on feedforward drive to fast-spiking (FS) interneurons, because pyramidal neurons can exhibit strong dendritic low-pass filtering ([Pike et al., 2000](#); [Buzsáki and Schomburg, 2015](#)). Several experimental studies have found that fast-spiking interneurons are more gamma-phase locked than (BW) E neurons ([Senzai et al., 2019](#); [Vinck et al., 2013a](#); [Csicsvari et al., 2003](#); [Hasenstaub et al., 2005](#); [Perrenoud et al., 2016](#); [Salkoff et al., 2015](#); [Vinck et al., 2016](#); [Schomburg et al., 2014](#); [Bragin et al., 1995](#)). In line with these findings, we found signatures of strong rhythmic inhibition in NW-burst neurons: first, we found that the discharge rates of NW-burst neurons were suppressed below pre-stimulus levels during their non-preferred gamma phase ([Figure 7](#)). This indicates an inhibitory input arriving at their non-preferred gamma phase. Second, we found that the discharge rates of most NW-burst neurons were suppressed at the non-preferred stimulus orientations. This suggests that they receive a broadly tuned inhibitory drive, which may sharpen their orientation tuning ([Shapley et al., 2003](#); [Kerlin et al., 2010](#); [Priebe and Ferster, 2008](#); [McLaughlin et al., 2000](#); [Isaacson and Scanziani, 2011](#)). Yet, despite this firing suppression for suboptimal stimuli, the gamma-phase locking of NW-burst neurons remained strong ([Figure 8](#)), indicating entrainment by rhythmic inhibition. If both orientation tuning and gamma-phase locking depend on inhibitory drive, then this might also explain why the most gamma-phase locked NW-burst neurons were the most orientation tuned ([Figure 8](#)). Further experiments are needed to reconcile these findings with the observed differences in gamma-phase locking among neuron

types in macaque V1. We found that putative fast-spiking interneurons (NW–nonburst neurons) had much lower gamma-phase locking than NW–burst neurons (Figure 6). In fact, their precision of phase locking was similar to BW neurons, although a few NW–nonburst neurons had strongly rhythmic side lobes in the autocorrelogram (Figure 2). These results are consistent with data from intracellular recordings in anesthetized cat V1 (Azouz et al., 1997), in which the autocorrelograms of most fast-spiking interneurons did not have prominent rhythmic side lobes. They also agree with previous observations that gamma-rhythmic firing in cat and monkey V1 is often accompanied by burst firing (Livingstone, 1996; Gray et al., 1990; Gray and Viana Di Prisco, 1997; Hubel and Wiesel, 1965; Friedman-Hill et al., 2000).

Although gamma synchronization likely reflects a generic dynamical motif emerging from recurrent E-I interactions, the strength and frequency bandwidth of gamma could be highly dependent on the specific properties of E neurons. These properties may vary across cortical areas, species, or laminae (Tasic et al., 2018; Senzai et al., 2019; Bernard et al., 2012). In most cortical systems, fast-spiking interneurons interact with BW E neurons that are regular spiking or irregularly bursting and exhibit low-pass filtering characteristics (Hasenstaub et al., 2005; Pike et al., 2000; Cardin et al., 2009). Experimental studies have found that E neurons with BWs are weakly phase locked compared to fast-spiking interneurons and fire in only a small percentage of gamma cycles (Hasenstaub et al., 2005; Csicsvari et al., 2003; Vinck et al., 2013a, 2016; Perrenoud et al., 2016; Senzai et al., 2019; Schomburg et al., 2014; Vinck et al., 2015). In fact, fast-spiking interneurons in mouse V1 and macaque V4 can sustain gamma-band oscillations despite very weak or no entrainment of E neurons, e.g., in the pre-stimulus baseline period (Perrenoud et al., 2016; Vinck et al., 2013a; Batista-Brito et al., 2017). In monkey and cat V1, however, the strong phase-locking and burst-firing properties of NW–burst neurons could lead to an amplification of gamma oscillations as compared to a circuit in which GABAergic interneurons interact predominantly with BW neurons with exclusively low-pass filtering characteristics.

This could potentially explain why V1 gamma oscillations in macaques and cats are particularly strong and narrow band: (1) spike-field locking values (PPC) in macaque V1 range between 0.05 and 0.15 during visual stimulation with gratings (Figure 6). In macaque V4 and rodent sensory cortex, gamma PPC values are typically smaller than ~0.005 (Vinck et al., 2013a, 2016; Perrenoud et al., 2016; van Wingerden et al., 2010). (2) The frequency range of gamma in cat and primate V1 is typically quite narrow (approximately ± 10 Hz) (Figures 5 and 6). In rodent S1 and V1, gamma-phase locking occurs in a broad frequency range (30–100 Hz) (Vinck et al., 2013a; Perrenoud et al., 2016; Vinck et al., 2016) (but see Veit et al., 2017, who reported a peak in the LFP at ~25–30 Hz in mouse V1). This is reflected in spike-triggered LFP averages and autocorrelograms that have rapidly decaying side lobes (Perrenoud et al., 2016; Vinck et al., 2016). (3) Many visual stimuli cause a very prominent increase in cat and monkey V1 gamma-band power as compared to pre-stimulus baseline. This increase can be as great as 10- to 300-fold (Brunet et al., 2014; Peter et al., 2019; Gray et al., 1989, 1990; Gray and Viana Di Prisco, 1997; Gieselmann and Thiele, 2008; Lima et al., 2010). In mouse V1, grating stimuli increase

LFP gamma power only by ~1.2- to 2-fold relative to baseline (Vinck et al., 2015; Perrenoud et al., 2016; Veit et al., 2017). The amplitude of monkey V1 gamma oscillations may be related to the size of area V1 and the RF sizes of V1 neurons; there is evidence that V1 gamma-synchronization reflects predictability among visual inputs across space (Vinck and Bosman, 2016; Peter et al., 2019). This hypothesis predicts high-amplitude gamma oscillations when RF sizes are small, as in the case of monkey V1, because predictability should be higher on small spatial scales (Vinck and Bosman, 2016). A complementary explanation is that when cortical networks are large, as is the case in cat and monkey V1 (large magnification factor and small RFs), reciprocal communication and cooperation between distal nodes may require strong oscillatory synchronization (Singer, 2018).

The properties of NW–burst neurons suggest that they have a particularly strong impact on post-synaptic targets: (1) burst firing can increase the gain and reliability of synaptic transmission and facilitate long-term potentiation (Lisman, 1997; Jackman and Regehr, 2017); and (2) synchronization of spikes can increase the gain of transmission to post-synaptic targets (Salinas and Sejnowski, 2000; Fries, 2015; Vinck et al., 2013b; Knoblich et al., 2010; Abeles, 1982; Palmigiano et al., 2017; König et al., 1996; Bernander et al., 1994; Kempter et al., 1998; Womelsdorf et al., 2007; Ni et al., 2016), and feedforward communication between visual areas is especially strong at gamma frequencies (Bastos et al., 2015; van Kerkoerle et al., 2014; Michalareas et al., 2016; Buschman and Miller, 2007; Gregoriou et al., 2009). Gamma synchronization is also associated with fast behavioral reaction times (Rohenkohl et al., 2018; Siegle et al., 2014; Womelsdorf et al., 2006). Further, gamma synchronization may have important consequences for spike-time-dependent plasticity (Vinck et al., 2010a; Sejnowski and Paulsen, 2006; Markram et al., 1997; unpublished data). Together with their high stimulus selectivity, this suggests that NW–burst neurons could be the principal source of communication with downstream target areas.

In sum, macaque V1 contains a specialized cell type that fires in high-frequency bursts, is strongly phase locked to gamma oscillations, and is highly stimulus selective. This neuron type is likely pivotal for the encoding and transmission of stimulus information. Through interactions with I neurons, these neurons could act as pacemaker for V1 gamma oscillations.

STAR★METHODS

Detailed methods are provided in the online version of this paper and include the following:

- KEY RESOURCES TABLE
- LEAD CONTACT AND MATERIALS AVAILABILITY
- EXPERIMENTAL MODEL AND SUBJECT DETAILS
- METHODS DETAILS
 - Surgical Procedures
 - Recordings
 - Behavioral Training and Task
 - Visual Stimulation Paradigm During Recordings
 - Recordings in Capuchin Monkeys

- Recordings in Mice
- Spike-Sorting
- QUANTIFICATION AND STATISTICAL ANALYSIS
 - Computation of the Autocorrelogram
 - Other Measurement of Burst-Propensity
 - Quantification of Spike-LFP Phase-Locking
 - Orientation and Direction Tuning
 - Simple versus Complex-Cell Modulation
 - Correlation between Firing Rate and Phase-Locking across Stimuli
 - Statistical Testing
- DATA AND CODE AVAILABILITY

SUPPLEMENTAL INFORMATION

Supplemental Information can be found online at <https://doi.org/10.1016/j.neuron.2019.09.039>.

ACKNOWLEDGMENTS

This work was supported by grants from the CNPq to S.N., who was supported by the FAPESP Research, Innovation and Dissemination Center for Neuromathematics. K.-S.R. received a scholarship from CAPES, PGNeuro, UFRN, Brazil. M.V. was supported by a BMF Computational Life Sciences grant.

AUTHOR CONTRIBUTIONS

Conceptualization, I.O. and M.V.; Methodology, I.O., S.N., J.H., B.L., K.-S.R., C.N., W.S., G.S., and M.V.; Software, I.O., S.N., and M.V.; Investigation, I.O., J.H., B.L., S.N., C.N., and M.V.; Writing – Original Draft, I.O. and M.V.; Writing – Review & Editing, all authors; Visualization, I.O. and M.V.; Supervision, M.V.

DECLARATION OF INTERESTS

The authors declare no competing interests.

Received: April 1, 2019

Revised: July 12, 2019

Accepted: September 23, 2019

Published: November 12, 2019

SUPPORTING CITATIONS

The following reference appears in the Supplemental Information: [Tao et al. \(2017\)](#).

REFERENCES

- Abeles, M. (1982). Role of the cortical neuron: integrator or coincidence detector? *Isr. J. Med. Sci.* **18**, 83–92.
- Ardid, S., Vinck, M., Kaping, D., Marquez, S., Everling, S., and Womelsdorf, T. (2015). Mapping of functionally characterized cell classes onto canonical circuit operations in primate prefrontal cortex. *J. Neurosci.* **35**, 2975–2991.
- Atallah, B.V., and Scanziani, M. (2009). Instantaneous modulation of gamma oscillation frequency by balancing excitation with inhibition. *Neuron* **62**, 566–577.
- Azouz, R., Gray, C., Nowak, L., and McCormick, D. (1997). Physiological properties of inhibitory interneurons in cat striate cortex. *Cereb. Cortex* **7**, 534–545.
- Balaram, P., and Kaas, J.H. (2014). Towards a unified scheme of cortical lamination for primary visual cortex across primates: insights from NeuN and VGLUT2 immunoreactivity. *Front. Neuroanat.* **8**, 81.
- Barthó, P., Hirase, H., Monconduit, L., Zugaro, M., Harris, K.D., and Buzsáki, G. (2004). Characterization of neocortical principal cells and interneurons by network interactions and extracellular features. *J. Neurophysiol.* **92**, 600–608.
- Bartos, M., Vida, I., and Jonas, P. (2007). Synaptic mechanisms of synchronized gamma oscillations in inhibitory interneuron networks. *Nat. Rev. Neurosci.* **8**, 45–56.
- Bastos, A.M., Vezoli, J., Bosman, C.A., Schoffelen, J.M., Oostenveld, R., Dowdall, J.R., De Weerd, P., Kennedy, H., and Fries, P. (2015). Visual areas exert feedforward and feedback influences through distinct frequency channels. *Neuron* **85**, 390–401.
- Batista-Brito, R., Vinck, M., Ferguson, K.A., Chang, J.T., Laubender, D., Lur, G., Mossner, J.M., Hernandez, V.G., Ramakrishnan, C., Deisseroth, K., et al. (2017). Developmental dysfunction of *vip* interneurons impairs cortical circuits. *Neuron* **95**, 884–895.e9.
- Batista-Brito, R., Zagha, E., Ratliff, J.M., and Vinck, M. (2018). Modulation of cortical circuits by top-down processing and arousal state in health and disease. *Curr. Opin. Neurobiol.* **52**, 172–181.
- Bernander, Ö., Koch, C., and Usher, M. (1994). The effect of synchronized inputs at the single neuron level. *Neural Comput.* **6**, 622–641.
- Bernard, A., Lubbers, L.S., Tanis, K.Q., Luo, R., Podtelezhnikov, A.A., Finney, E.M., McWhorter, M.M., Serikawa, K., Lemon, T., Morgan, R., et al. (2012). Transcriptional architecture of the primate neocortex. *Neuron* **73**, 1083–1099.
- Besserve, M., Lowe, S.C., Logothetis, N.K., Schölkopf, B., and Panzeri, S. (2015). Shifts of gamma phase across primary visual cortical sites reflect dynamic stimulus-modulated information transfer. *PLoS Biol.* **13**, e1002257.
- Börgers, C., and Kopell, N. (2005). Effects of noisy drive on rhythms in networks of excitatory and inhibitory neurons. *Neural Comput.* **17**, 557–608.
- Börgers, C., and Kopell, N.J. (2008). Gamma oscillations and stimulus selection. *Neural Comput.* **20**, 383–414.
- Bragin, A., Jandó, G., Nádasdy, Z., Hetke, J., Wise, K., and Buzsáki, G. (1995). Gamma (40–100 Hz) oscillation in the hippocampus of the behaving rat. *J. Neurosci.* **15**, 47–60.
- Brunet, N.M., Bosman, C.A., Vinck, M., Roberts, M., Oostenveld, R., Desimone, R., De Weerd, P., and Fries, P. (2014). Stimulus repetition modulates gamma-band synchronization in primate visual cortex. *Proc. Natl. Acad. Sci. USA* **111**, 3626–3631.
- Buffalo, E.A., Fries, P., Landman, R., Buschman, T.J., and Desimone, R. (2011). Laminar differences in gamma and alpha coherence in the ventral stream. *Proc. Natl. Acad. Sci. USA* **108**, 11262–11267.
- Buschman, T.J., and Miller, E.K. (2007). Top-down versus bottom-up control of attention in the prefrontal and posterior parietal cortices. *Science* **315**, 1860–1862.
- Bush, P., and Sejnowski, T. (1996). Inhibition synchronizes sparsely connected cortical neurons within and between columns in realistic network models. *J. Comput. Neurosci.* **3**, 91–110.
- Buzsáki, G. (2006). *Rhythms of the Brain* (Oxford University Press).
- Buzsáki, G., and Schomburg, E.W. (2015). What does gamma coherence tell us about inter-regional neural communication? *Nat. Neurosci.* **18**, 484–489.
- Buzsáki, G., and Wang, X.J. (2012). Mechanisms of gamma oscillations. *Annu. Rev. Neurosci.* **35**, 203–225.
- Cardin, J.A., Palmer, L.A., and Contreras, D. (2005). Stimulus-dependent gamma (30–50 Hz) oscillations in simple and complex fast rhythmic bursting cells in primary visual cortex. *J. Neurosci.* **25**, 5339–5350.
- Cardin, J.A., Carlén, M., Meletis, K., Knoblich, U., Zhang, F., Deisseroth, K., Tsai, L.H., and Moore, C.I. (2009). Driving fast-spiking cells induces gamma rhythm and controls sensory responses. *Nature* **459**, 663–667.
- Chalk, M., Herrero, J.L., Gieselmann, M.A., Delicato, L.S., Gotthardt, S., and Thiele, A. (2010). Attention reduces stimulus-driven gamma frequency oscillations and spike field coherence in V1. *Neuron* **66**, 114–125.
- Chen, G., Zhang, Y., Li, X., Zhao, X., Ye, Q., Lin, Y., Tao, H.W., Rasch, M.J., and Zhang, X. (2017). Distinct inhibitory circuits orchestrate cortical beta and gamma band oscillations. *Neuron* **96**, 1403–1418.e6.
- Constantinople, C.M., Disney, A.A., Maffie, J., Rudy, B., and Hawken, M.J. (2009). Quantitative analysis of neurons with Kv3 potassium channel subunits,

- Kv3.1b and Kv3.2, in macaque primary visual cortex. *J. Comp. Neurol.* 516, 291–311.
- Csicsvari, J., Hirase, H., Czurkó, A., Mamiya, A., and Buzsáki, G. (1999). Oscillatory coupling of hippocampal pyramidal cells and interneurons in the behaving Rat. *J. Neurosci.* 19, 274–287.
- Csicsvari, J., Jamieson, B., Wise, K.D., and Buzsáki, G. (2003). Mechanisms of gamma oscillations in the hippocampus of the behaving rat. *Neuron* 37, 311–322.
- Friedman-Hill, S., Maldonado, P.E., and Gray, C.M. (2000). Dynamics of striate cortical activity in the alert macaque: I. Incidence and stimulus-dependence of gamma-band neuronal oscillations. *Cereb. Cortex* 10, 1105–1116.
- Fries, P. (2009). Neuronal gamma-band synchronization as a fundamental process in cortical computation. *Annu. Rev. Neurosci.* 32, 209–224.
- Fries, P. (2015). Rhythms for cognition: communication through coherence. *Neuron* 88, 220–235.
- Gentet, L.J. (2012). Functional diversity of supragranular GABAergic neurons in the barrel cortex. *Front. Neural Circuits* 6, 52.
- Gentet, L.J., Kremer, Y., Taniguchi, H., Huang, Z.J., Staiger, J.F., and Petersen, C.C. (2012). Unique functional properties of somatostatin-expressing GABAergic neurons in mouse barrel cortex. *Nat. Neurosci.* 15, 607–612.
- Gieselmann, M.A., and Thiele, A. (2008). Comparison of spatial integration and surround suppression characteristics in spiking activity and the local field potential in macaque V1. *Eur. J. Neurosci.* 28, 447–459.
- Gray, C.M., and McCormick, D.A. (1996). Chattering cells: superficial pyramidal neurons contributing to the generation of synchronous oscillations in the visual cortex. *Science* 274, 109–113.
- Gray, C.M., and Viana Di Prisco, G. (1997). Stimulus-dependent neuronal oscillations and local synchronization in striate cortex of the alert cat. *J. Neurosci.* 17, 3239–3253.
- Gray, C.M., König, P., Engel, A.K., and Singer, W. (1989). Oscillatory responses in cat visual cortex exhibit inter-columnar synchronization which reflects global stimulus properties. *Nature* 338, 334–337.
- Gray, C.M., Engel, A.K., König, P., and Singer, W. (1990). Stimulus-dependent neuronal oscillations in cat visual cortex: Receptive field properties and feature dependence. *Eur. J. Neurosci.* 2, 607–619.
- Gray, C.M., Engel, A.K., König, P., and Singer, W. (1992). Synchronization of oscillatory neuronal responses in cat striate cortex: temporal properties. *Vis. Neurosci.* 8, 337–347.
- Gregoriou, G.G., Gotts, S.J., Zhou, H., and Desimone, R. (2009). High-frequency, long-range coupling between prefrontal and visual cortex during attention. *Science* 324, 1207–1210.
- Gur, M., Beylin, A., and Snodderly, D.M. (1999). Physiological properties of macaque V1 neurons are correlated with extracellular spike amplitude, duration, and polarity. *J. Neurophysiol.* 82, 1451–1464.
- Haider, B., and McCormick, D.A. (2009). Rapid neocortical dynamics: cellular and network mechanisms. *Neuron* 62, 171–189.
- Haider, B., Krause, M.R., Duque, A., Yu, Y., Touryan, J., Mazer, J.A., and McCormick, D.A. (2010). Synaptic and network mechanisms of sparse and reliable visual cortical activity during nonclassical receptive field stimulation. *Neuron* 65, 107–121.
- Hasenstaub, A., Shu, Y., Haider, B., Kraushaar, U., Duque, A., and McCormick, D.A. (2005). Inhibitory postsynaptic potentials carry synchronized frequency information in active cortical networks. *Neuron* 47, 423–435.
- Hässler, R. (1966). Comparative anatomy of the central visual systems in day- and night-active primates. In *Evolution of the Forebrain* (Springer), pp. 419–434.
- Hendry, S.H., Schwark, H.D., Jones, E.G., and Yan, J. (1987). Numbers and proportions of GABA-immunoreactive neurons in different areas of monkey cerebral cortex. *J. Neurosci.* 7, 1503–1519.
- Henrie, J.A., and Shapley, R. (2005). LFP power spectra in V1 cortex: the graded effect of stimulus contrast. *J. Neurophysiol.* 94, 479–490.
- Herculano-Houzel, S., Munk, M.H., Neuenschwander, S., and Singer, W. (1999). Precisely synchronized oscillatory firing patterns require electroencephalographic activation. *J. Neurosci.* 19, 3992–4010.
- Hoy, J.L., and Niell, C.M. (2015). Layer-specific refinement of visual cortex function after eye opening in the awake mouse. *J. Neurosci.* 35, 3370–3383.
- Hubel, D.H., and Wiesel, T.N. (1965). Receptive fields and functional architecture in two nonstriate visual areas (18 and 19) of the cat. *J. Neurophysiol.* 28, 229–289.
- Isaacson, J.S., and Scanziani, M. (2011). How inhibition shapes cortical activity. *Neuron* 72, 231–243.
- Jackman, S.L., and Regehr, W.G. (2017). The mechanisms and functions of synaptic facilitation. *Neuron* 94, 447–464.
- Jadi, M.P., and Sejnowski, T.J. (2014). Cortical oscillations arise from contextual interactions that regulate sparse coding. *Proc. Natl. Acad. Sci. USA* 111, 6780–6785.
- Jagadeesh, B., Gray, C.M., and Ferster, D. (1992). Visually evoked oscillations of membrane potential in cells of cat visual cortex. *Science* 257, 552–554.
- Jia, X., Smith, M.A., and Kohn, A. (2011). Stimulus selectivity and spatial coherence of gamma components of the local field potential. *J. Neurosci.* 31, 9390–9403.
- Jia, X., Xing, D., and Kohn, A. (2013). No consistent relationship between gamma power and peak frequency in macaque primary visual cortex. *J. Neurosci.* 33, 17–25.
- Jouhanneau, J.S., Kremkow, J., and Poulet, J.F.A. (2018). Single synaptic inputs drive high-precision action potentials in parvalbumin expressing GABAergic cortical neurons *in vivo*. *Nat. Commun.* 9, 1540.
- Kempter, R., Gerstner, W., van Hemmen, J.L., and Wagner, H. (1998). Extracting oscillations. Neuronal coincidence detection with noisy periodic spike input. *Neural Comput.* 10, 1987–2017.
- Kerlin, A.M., Andermann, M.L., Berezovskii, V.K., and Reid, R.C. (2010). Broadly tuned response properties of diverse inhibitory neuron subtypes in mouse visual cortex. *Neuron* 67, 858–871.
- Knoblich, U., Siegle, J.H., Pritchett, D.L., and Moore, C.I. (2010). What do we gain from gamma? Local dynamic gain modulation drives enhanced efficacy and efficiency of signal transmission. *Front. Hum. Neurosci.* 4, 185.
- König, P., Engel, A.K., and Singer, W. (1996). Integrator or coincidence detector? The role of the cortical neuron revisited. *Trends Neurosci.* 19, 130–137.
- Kopell, N., Ermentrout, G.B., Whittington, M.A., and Traub, R.D. (2000). Gamma rhythms and beta rhythms have different synchronization properties. *Proc. Natl. Acad. Sci. USA* 97, 1867–1872.
- Lima, B., Singer, W., Chen, N.H., and Neuenschwander, S. (2010). Synchronization dynamics in response to plaid stimuli in monkey V1. *Cereb. Cortex* 20, 1556–1573.
- Lisman, J.E. (1997). Bursts as a unit of neural information: making unreliable synapses reliable. *Trends Neurosci.* 20, 38–43.
- Livingstone, M.S. (1996). Oscillatory firing and interneuronal correlations in squirrel monkey striate cortex. *J. Neurophysiol.* 75, 2467–2485.
- Lytton, W.W., and Sejnowski, T.J. (1991). Simulations of cortical pyramidal neurons synchronized by inhibitory interneurons. *J. Neurophysiol.* 66, 1059–1079.
- Maldonado, P.E., Friedman-Hill, S., and Gray, C.M. (2000). Dynamics of striate cortical activity in the alert macaque: II. Fast time scale synchronization. *Cereb. Cortex* 10, 1117–1131.
- Maris, E., and Oostenveld, R. (2007). Nonparametric statistical testing of EEG and MEG data. *J. Neurosci. Methods* 164, 177–190.
- Markram, H., Lübke, J., Frotscher, M., and Sakmann, B. (1997). Regulation of synaptic efficacy by coincidence of postsynaptic APs and EPSPs. *Science* 275, 213–215.
- Markram, H., Toledo-Rodriguez, M., Wang, Y., Gupta, A., Silberberg, G., and Wu, C. (2004). Interneurons of the neocortical inhibitory system. *Nat. Rev. Neurosci.* 5, 793–807.

- Martinez, L.M., and Alonso, J.M. (2003). Complex receptive fields in primary visual cortex. *Neuroscientist* 9, 317–331.
- McCormick, D.A., Connors, B.W., Lighthill, J.W., and Prince, D.A. (1985). Comparative electrophysiology of pyramidal and sparsely spiny stellate neurons of the neocortex. *J. Neurophysiol.* 54, 782–806.
- McGinley, M.J., David, S.V., and McCormick, D.A. (2015a). Cortical membrane potential signature of optimal states for sensory signal detection. *Neuron* 87, 179–192.
- McGinley, M.J., Vinck, M., Reimer, J., Batista-Brito, R., Zagha, E., Cadwell, C.R., Tolias, A.S., Cardin, J.A., and McCormick, D.A. (2015b). Waking state: rapid variations modulate neural and behavioral responses. *Neuron* 87, 1143–1161.
- McLaughlin, D., Shapley, R., Shelley, M., and Wieland, D.J. (2000). A neuronal network model of macaque primary visual cortex (V1): orientation selectivity and dynamics in the input layer 4Calpha. *Proc. Natl. Acad. Sci. USA* 97, 8087–8092.
- Michalareas, G., Vezoli, J., van Pelt, S., Schoffelen, J.M., Kennedy, H., and Fries, P. (2016). Alpha-beta and gamma rhythms subserve feedback and feed-forward influences among human visual cortical areas. *Neuron* 89, 384–397.
- Miri, M.L., Vinck, M., Pant, R., and Cardin, J.A. (2018). Altered hippocampal interneuron activity precedes ictal onset. *eLife* 7, e40750.
- Mitchell, J.F., Sundberg, K.A., and Reynolds, J.H. (2007). Differential attention-dependent response modulation across cell classes in macaque visual area V4. *Neuron* 55, 131–141.
- Moore, C.I., Carlen, M., Knoblich, U., and Cardin, J.A. (2010). Neocortical interneurons: from diversity, strength. *Cell* 142, 189–193.
- Ni, J., Wunderle, T., Lewis, C.M., Desimone, R., Diester, I., and Fries, P. (2016). Gamma-rhythmic gain modulation. *Neuron* 92, 240–251.
- Niell, C.M., and Stryker, M.P. (2010). Modulation of visual responses by behavioral state in mouse visual cortex. *Neuron* 65, 472–479.
- Nowak, L.G., Azouz, R., Sanchez-Vives, M.V., Gray, C.M., and McCormick, D.A. (2003). Electrophysiological classes of cat primary visual cortical neurons in vivo as revealed by quantitative analyses. *J. Neurophysiol.* 89, 1541–1566.
- Nowak, L.G., Sanchez-Vives, M.V., and McCormick, D.A. (2008). Lack of orientation and direction selectivity in a subgroup of fast-spiking inhibitory interneurons: cellular and synaptic mechanisms and comparison with other electrophysiological cell types. *Cereb. Cortex* 18, 1058–1078.
- Ohki, K., and Reid, R.C. (2007). Specificity and randomness in the visual cortex. *Curr. Opin. Neurobiol.* 17, 401–407.
- Oostenveld, R., Fries, P., Maris, E., and Schoffelen, J.M. (2011). FieldTrip: open source software for advanced analysis of MEG, EEG, and invasive electrophysiological data. *Comput. Intell. Neurosci.* 2011, 156869.
- Palmigiano, A., Geisel, T., Wolf, F., and Battaglia, D. (2017). Flexible information routing by transient synchrony. *Nat. Neurosci.* 20, 1014–1022.
- Perrenoud, Q., Pennartz, C.M., and Gentet, L.J. (2016). Membrane potential dynamics of spontaneous and visually evoked gamma activity in V1 of awake mice. *PLoS Biol.* 14, e1002383.
- Pesaran, B., Vinck, M., Einevoll, G.T., Sirota, A., Fries, P., Siegel, M., Truccolo, W., Schroeder, C.E., and Srinivasan, R. (2018). Investigating large-scale brain dynamics using field potential recordings: analysis and interpretation. *Nat. Neurosci.* 21, 903–919.
- Peter, A., Uran, C., Klon-Lipok, J., Roese, R., van Stijn, S., Barnes, W., Dowdall, J.R., Singer, W., Fries, P., and Vinck, M. (2019). Surface color and predictability determine contextual modulation of V1 firing and gamma oscillations. *eLife* 8, e42101.
- Pike, F.G., Goddard, R.S., Suckling, J.M., Ganter, P., Kasthuri, N., and Paulsen, O. (2000). Distinct frequency preferences of different types of rat hippocampal neurones in response to oscillatory input currents. *J. Physiol.* 529, 205–213.
- Priebe, N.J., and Ferster, D. (2008). Inhibition, spike threshold, and stimulus selectivity in primary visual cortex. *Neuron* 57, 482–497.
- Ray, S., and Maunsell, J.H.R. (2010). Differences in gamma frequencies across visual cortex restrict their possible use in computation. *Neuron* 67, 885–896.
- Roberts, M.J., Lowet, E., Brunet, N.M., Ter Wal, M., Tiesinga, P., Fries, P., and De Weerd, P. (2013). Robust gamma coherence between macaque V1 and V2 by dynamic frequency matching. *Neuron* 78, 523–536.
- Rohenkohl, G., Bosman, C.A., and Fries, P. (2018). Gamma synchronization between V1 and V4 improves behavioral performance. *Neuron* 100, 953–963.e3.
- Rudy, B., Fishell, G., Lee, S., and Hjerling-Leffler, J. (2011). Three groups of interneurons account for nearly 100% of neocortical GABAergic neurons. *Dev. Neurobiol.* 71, 45–61.
- Salinas, E., and Sejnowski, T.J. (2000). Impact of correlated synaptic input on output firing rate and variability in simple neuronal models. *J. Neurosci.* 20, 6193–6209.
- Salkoff, D.B., Zagha, E., Yüzgeç, Ö., and McCormick, D.A. (2015). Synaptic mechanisms of tight spike synchrony at gamma frequency in cerebral cortex. *J. Neurosci.* 35, 10236–10251.
- Schmitzer-Torbert, N., Jackson, J., Henze, D., Harris, K., and Redish, A.D. (2005). Quantitative measures of cluster quality for use in extracellular recordings. *Neuroscience* 131, 1–11.
- Schomburg, E.W., Fernández-Ruiz, A., Mizuseki, K., Berényi, A., Anastassiou, C.A., Koch, C., and Buzsáki, G. (2014). Theta phase segregation of input-specific gamma patterns in entorhinal-hippocampal networks. *Neuron* 84, 470–485.
- Sejnowski, T.J., and Paulsen, O. (2006). Network oscillations: emerging computational principles. *J. Neurosci.* 26, 1673–1676.
- Senzai, Y., Fernandez-Ruiz, A., and Buzsáki, G. (2019). Layer-specific physiological features and interlaminar interactions in the primary visual cortex of the mouse. *Neuron* 101, 500–513.e5.
- Shapley, R., Hawken, M., and Ringach, D.L. (2003). Dynamics of orientation selectivity in the primary visual cortex and the importance of cortical inhibition. *Neuron* 38, 689–699.
- Siegle, J.H., Pritchett, D.L., and Moore, C.I. (2014). Gamma-range synchronization of fast-spiking interneurons can enhance detection of tactile stimuli. *Nat. Neurosci.* 17, 1371–1379.
- Singer, W. (2018). Neuronal oscillations: unavoidable and useful? *Eur. J. Neurosci.* 48, 2389–2398.
- Singer, W., and Gray, C.M. (1995). Visual feature integration and the temporal correlation hypothesis. *Annu. Rev. Neurosci.* 18, 555–586.
- Sirota, A., Montgomery, S., Fujisawa, S., Isomura, Y., Zugaro, M., and Buzsáki, G. (2008). Entrainment of neocortical neurons and gamma oscillations by the hippocampal theta rhythm. *Neuron* 60, 683–697.
- Sohal, V.S., Zhang, F., Yizhar, O., and Deisseroth, K. (2009). Parvalbumin neurons and gamma rhythms enhance cortical circuit performance. *Nature* 459, 698–702.
- Steriade, M., Timofeev, I., Dürmüller, N., and Grenier, F. (1998). Dynamic properties of corticothalamic neurons and local cortical interneurons generating fast rhythmic (30–40 Hz) spike bursts. *J. Neurophysiol.* 79, 483–490.
- Steriade, M., Timofeev, I., and Grenier, F. (2001). Natural waking and sleep states: a view from inside neocortical neurons. *J. Neurophysiol.* 85, 1969–1985.
- Tao, X., Zhou, C., Shen, X., Wang, J., and Jia, J. (2017). Zero-order reverse filtering. In Proceedings of the IEEE International Conference on Computer Vision, pp. 222–230.
- Tasic, B., Yao, Z., Graybuck, L.T., Smith, K.A., Nguyen, T.N., Bertagnolli, D., Goldy, J., Garren, E., Economo, M.N., Viswanathan, S., et al. (2018). Shared and distinct transcriptomic cell types across neocortical areas. *Nature* 563, 72–78.
- Tiesinga, P., and Sejnowski, T.J. (2009). Cortical enlightenment: are attentional gamma oscillations driven by ING or PING? *Neuron* 63, 727–732.

- Trainito, C., von Nicolai, C., Miller, E.K., and Siegel, M. (2019). Extracellular spike waveform dissociates four functionally distinct cell classes in primate cortex. *Curr. Biol.* 29, 2973–2982.e5.
- van Kerkoerle, T., Self, M.W., Dagnino, B., Gariel-Mathis, M.A., Poort, J., van der Togt, C., and Roelfsema, P.R. (2014). Alpha and gamma oscillations characterize feedback and feedforward processing in monkey visual cortex. *Proc. Natl. Acad. Sci. USA* 111, 14332–14341.
- van Wingerden, M., Vinck, M., Lankelma, J.V., and Pennartz, C.M. (2010). Learning-associated gamma-band phase-locking of action-outcome selective neurons in orbitofrontal cortex. *J. Neurosci.* 30, 10025–10038.
- Veit, J., Hakim, R., Jadi, M.P., Sejnowski, T.J., and Adesnik, H. (2017). Cortical gamma band synchronization through somatostatin interneurons. *Nat. Neurosci.* 20, 951–959.
- Vinck, M., and Bosman, C.A. (2016). More gamma more predictions: gamma-synchronization as a key mechanism for efficient integration of classical receptive field inputs with surround predictions. *Front. Syst. Neurosci.* 10, 35.
- Vinck, M., Lima, B., Womelsdorf, T., Oostenveld, R., Singer, W., Neuenschwander, S., and Fries, P. (2010a). Gamma-phase shifting in awake monkey visual cortex. *J. Neurosci.* 30, 1250–1257.
- Vinck, M., van Wingerden, M., Womelsdorf, T., Fries, P., and Pennartz, C.M. (2010b). The pairwise phase consistency: a bias-free measure of rhythmic neuronal synchronization. *Neuroimage* 51, 112–122.
- Vinck, M., Battaglia, F.P., Womelsdorf, T., and Pennartz, C. (2012). Improved measures of phase-coupling between spikes and the local field potential. *J. Comput. Neurosci.* 33, 53–75.
- Vinck, M., Womelsdorf, T., Buffalo, E.A., Desimone, R., and Fries, P. (2013a). Attentional modulation of cell-class-specific gamma-band synchronization in awake monkey area v4. *Neuron* 80, 1077–1089.
- Vinck, M., Womelsdorf, T., and Fries, P. (2013b). Gamma-band synchronization and information transmission. In *Principles of Neural Coding*, R. Quiroga-Quian and S. Panzeri, eds. (CRC Press).
- Vinck, M., Batista-Brito, R., Knoblich, U., and Cardin, J.A. (2015). Arousal and locomotion make distinct contributions to cortical activity patterns and visual encoding. *Neuron* 86, 740–754.
- Vinck, M., Bos, J.J., Van Mourik-Donga, L.A., Oplaat, K.T., Klein, G.A., Jackson, J.C., Gentet, L.J., and Pennartz, C.M. (2016). Cell-type and state-dependent synchronization among rodent somatosensory, visual, perirhinal cortex, and hippocampus ca1. *Front. Syst. Neurosci.* 9, 187.
- Wang, X.J. (1999). Fast burst firing and short-term synaptic plasticity: a model of neocortical chattering neurons. *Neuroscience* 89, 347–362.
- Wang, X.J. (2010). Neurophysiological and computational principles of cortical rhythms in cognition. *Physiol. Rev.* 90, 1195–1268.
- Wang, X.J., and Buzsáki, G. (1996). Gamma oscillation by synaptic inhibition in a hippocampal interneuronal network model. *J. Neurosci.* 16, 6402–6413.
- Whittington, M.A., Traub, R.D., and Jefferys, J.G. (1995). Synchronized oscillations in interneuron networks driven by metabotropic glutamate receptor activation. *Nature* 373, 612–615.
- Whittington, M.A., Traub, R.D., Kopell, N., Ermentrout, B., and Buhl, E.H. (2000). Inhibition-based rhythms: experimental and mathematical observations on network dynamics. *Int. J. Psychophysiol.* 38, 315–336.
- Whittington, M.A., Cunningham, M.O., LeBeau, F.E., Racca, C., and Traub, R.D. (2011). Multiple origins of the cortical γ rhythm. *Dev. Neurobiol.* 71, 92–106.
- Wilson, D.E., Scholl, B., and Fitzpatrick, D. (2018). Differential tuning of excitation and inhibition shapes direction selectivity in ferret visual cortex. *Nature* 560, 97–101.
- Womelsdorf, T., Fries, P., Mitra, P.P., and Desimone, R. (2006). Gamma-band synchronization in visual cortex predicts speed of change detection. *Nature* 439, 733–736.
- Womelsdorf, T., Schoffelen, J.M., Oostenveld, R., Singer, W., Desimone, R., Engel, A.K., and Fries, P. (2007). Modulation of neuronal interactions through neuronal synchronization. *Science* 316, 1609–1612.
- Womelsdorf, T., Lima, B., Vinck, M., Oostenveld, R., Singer, W., Neuenschwander, S., and Fries, P. (2012). Orientation selectivity and noise correlation in awake monkey area V1 are modulated by the gamma cycle. *Proc. Natl. Acad. Sci. USA* 109, 4302–4307.
- Womelsdorf, T., Valiante, T.A., Sahin, N.T., Miller, K.J., and Tiesinga, P. (2014). Dynamic circuit motifs underlying rhythmic gain control, gating and integration. *Nat. Neurosci.* 17, 1031–1039.
- Xing, D., Yeh, C.I., Burns, S., and Shapley, R.M. (2012). Laminar analysis of visually evoked activity in the primary visual cortex. *Proc. Natl. Acad. Sci. USA* 109, 13871–13876.
- Zagha, E., Casale, A.E., Sachdev, R.N., McGinley, M.J., and McCormick, D.A. (2013). Motor cortex feedback influences sensory processing by modulating network state. *Neuron* 79, 567–578.
- Znamenskiy, P., Kim, M.H., Muir, D.R., Iacaruso, M.F., Hofer, S.B., and Mrsic-Flogel, T.D. (2018). Functional selectivity and specific connectivity of inhibitory neurons in primary visual cortex. *bioRxiv*. <https://doi.org/10.1101/294835>.

STAR★METHODS

KEY RESOURCES TABLE

REAGENT or RESOURCE	SOURCE	IDENTIFIER
Experimental Models: Organisms/Strains		
Rhesus macaques (<i>macaca mulatta</i>)	German Primate Centrum, Germany & Aventis Pharma Deutschland GmbH, Germany	NA
Capuchin monkey (<i>Sapajus libidinosus</i>)	IBAMA-Natal, Brazil	IBRN-13 (982009106551523)
C57BL/6J mice	The Jackson Laboratory	NA
Software and Algorithms		
MATLAB	Mathworks	https://www.mathworks.com/
FieldTrip Toolbox	Oostenveld et al., 2011	http://www.fieldtriptoolbox.org

LEAD CONTACT AND MATERIALS AVAILABILITY

The Lead Contact of this study is Martin Vinck. Further information and requests for resources should be directed to and will be fulfilled by the Lead Contact, Martin Vinck (martin.vinck@esi-frankfurt.de). This study did not generate new unique reagents.

EXPERIMENTAL MODEL AND SUBJECT DETAILS

For the data collected in macaque V1, one male and one female adult rhesus monkey (*macaca mullata*) served as subjects. Their ages and weights at the start of recordings were 11 and 17 years and 11.5 and 8.5 kg. All procedures complied with the guidelines of the European Community for the care and use of laboratory animals (European Union Directive 86/609/EEC). The experiments were approved by the regional authority for animal welfare (Regierungspräsidium Hessen, Darmstadt, Germany).

For the data collected in mice, adult male and female C57BL/6J mice served as subjects (age range 2–4 months). Mice were maintained on a 14/10 h light/dark cycle and recordings were performed 34 h before the start of their normal dark (awake) cycle. Experiments in mice were conducted with approved protocols from the University of Oregon Institutional Animal Care and Use Committees, in compliance with National Institutes of Health guidelines for the care and use of experimental animals.

For the data collected in capuchin monkey (*Sapajus libidinosus*), one male capuchin monkey served as subject (9 years old and 3.1 kg at start of recording). All procedures related to recordings in capuchin monkeys were approved by the Ethics Committee of the Federal University of Rio Grande do Norte (Protocol number 053/2012, CEUA) and Biodiversity Authorization and Information System (SISBIO 35425-2).

METHODS DETAILS

Surgical Procedures

Recordings were made from two adult rhesus-monkeys (*Macaca mulatta*). We performed surgical procedures under general anesthesia and provided analgesic treatment after the operations. In each monkey, we implanted a titanium headpost, which was later used for head fixation, and a titanium recording chamber. We inserted 2 to 10 microelectrodes independently into the cortex via transdural guide tubes (diameter: 300 µm; Ehrhardt Soehne). These electrodes had distances to each other between 1 and 3 mm and were made of quartz-insulated, tungstenplatinum material (diameter: 80 µm; impedances between 0.3 and 1 MΩ; Thomas Recording). We recorded from superficial layers in the opercular region of V1. The receptive-field centers of the units had eccentricities between 2 and 3 degrees of visual angle.

Recordings

Electrode signals were amplified (1000x) and filtered using a 32-channel head-stage amplifier (head stage HST16o25; head stage and preamplifier from Plexon). The filter-ranges for multi-unit activity and LFPs (Pesaran et al., 2018) were 0.7–6 kHz (2nd and 4th order Butterworth) and 0.7–170 Hz (2nd and 4th order Butterworth), respectively. An on-board acquisition board provided an additional 10x amplification (E-series acquisition boards; National Instruments). The signals were digitized and stored with a LabVIEW-based acquisition system (written by SN). To detect spikes, we manually set a threshold based on online visualization of the spike waveforms. This threshold was typically between 2 and 3 SDs above the noise level. LFP signals and spike waveforms were sampled at 1 kHz and

32kHz, respectively. The eye position was monitored either with a search coil system (DNI, Crist Instruments, USA; temporal resolution of 2 ms) or with an infrared eye tracker (temporal resolution of 33 ms).

Behavioral Training and Task

We trained both monkeys on a fixation task. At the start of each trial, a square, red fixation-dot appeared on the monitor (0.15 degrees; 4 × 4 pixels; luminance: 10.0 cd/m²). The monkeys then had to press a lever, and maintain their gaze within a radius of ≈0.5 degrees of visual angle from the center of the fixation point. After a random interval within 2500–4000ms, the color of the fixation dot changed from red to green. The monkey could then obtain a reward by releasing the lever between 200 and 500ms after the color change. A trial was aborted if, before the color change, the monkey released the lever or moved his eyes outside the fixation window. The monkeys typically performed between 700 and 1500 correct trials in a 4-h session.

Visual Stimulation Paradigm During Recordings

We used an interface in LabVIEW (written by SN; LabVIEW, National Instruments, USA) to generate stimuli as sequences of bitmap images. The stimuli were presented as movies with a resolution of 1024 × 768 pixels and a frame rate of 100–120Hz. We controlled the stimulus presentation with a graphical board (GeForce 6600-series, NVIDIA, Santa Clara, CA) and the ActiveStim software (www.activestim.com). With the ActiveStim software, we achieved accurate timing and a stimulus-onset jitter below 1ms. The movies were displayed on a cathode-ray-tube monitor (CM813ET, Hitachi, Japan), which was 36 × 28 degrees of visual angle wide (1024 × 768 pixels). We gamma-corrected this monitor, such that the relationship between output luminance and gray values was linear.

At the beginning of each recording session, we presented moving bar-stimuli in 16 different directions. We analyzed the neural responses to these bar stimuli in order to estimate the RFs of the recorded units. We then proceeded with the presentation of drifting-grating stimuli, which were centered on the RFs. Each trial started with a pre-stimulus baseline of 800–1000ms, followed by the presentation of a drifting-grating stimulus for a duration of 800–1500ms. The stimulus duration was constant in a given recording session. The drifting gratings had spatial frequencies of 1.25–2 cycles per degree, and temporal frequencies of 1.4–2 cycles per second. In each trial, the direction of the grating drift was orthogonal to grating orientation and randomly chosen from 16 directions (in steps of 22.5 degrees). During the presentation of visual stimuli, the monkeys performed a fixation task as described above, for which the stimuli had no behavioral relevance.

Recordings in Capuchin Monkeys

Additional data were obtained from recordings in one capuchin monkey (*Sapajus libidinosus*). Capuchins were required to maintain fixation continuously for 2000 to 3000 ms. Different from the experiments with the macaque monkeys, the capuchins were not required to press a lever. All other procedures (electrodes, recording devices, acquisition, and stimulation systems) were identical between the two experiments.

Recordings in Mice

The details for recordings in mice are described in detail in ([Hoy and Niell, 2015](#)). We recorded from area V1 in awake, adult head-fixed C57BL/6J mice placed on a spherical treadmill ([Niell and Stryker, 2010](#)). Recordings were made with two-shank 32-channel silicon probes having 25 μm spacing between channels (Neuronexus). Electrodes were coated in DiO, which we used for identification of the laminar position of the electrodes. Data acquisition was performed using the TDT System 3 workstation. We presented full-field drifting-grating stimuli with spatial frequencies between 0.01 and 0.32 (0.01, 0.02, 0.04, 0.08, 0.16, 0.32) and 16 different drift-directions. The extracellular signal was filtered between 0.3 to 7 kHz (2nd order Butterworth) and stored at 25 kHz. We detected spiking events online by voltage threshold crossings. For each spike, we stored a 1 ms waveform sample on four adjacent recording surfaces, which formed a “virtual” tetrode that was then used for spike sorting. We performed single-unit clustering and spike-waveform analysis as described in [Niell and Stryker \(2010\)](#); [Hoy and Niell \(2015\)](#).

Spike-Sorting

We performed semi-automated spike sorting to isolate neurons. For automatic clustering, we used the KlustaKwik 3.0 software. The features used were the energy of the spike waveform, and the energy of the waveform’s first derivative. Based on the results of the automatic clustering, we manually sorted units with the M-Clust software. We accepted units only if a clear separation of the cell relative to the noise clusters was observed, and if the inter-spike-interval distribution had a clear refractory-period. This was generally the case when a conventional measure of cluster separation, isolation distance (ID) exceeded 20 ([Schmitzer-Torbert et al., 2005](#)) (the median ID was 25.05). NW-Burst and NW-Nonburst neurons did not significantly differ in the ID ($P > 0.05$).

QUANTIFICATION AND STATISTICAL ANALYSIS

We analyzed the data in MATLAB by using the FieldTrip toolbox ([Oostenveld et al., 2011](#)) and custom-made scripts (IO and MV). We included only correct trials into our analyses.

Computation of the Autocorrelogram

We computed the autocorrelogram separately for the stimulus period (>200ms after stimulus onset) and the pre-stimulus period. The autocorrelogram was computed by sampling the spike trains at 2000Hz and convolving them with themselves. This corresponds to counting the number of times that a pair of spikes has a certain delay. We corrected the autocorrelogram for bias due to finite analysis periods. We estimated the time at which the autocorrelogram reached a global peak with the following procedure:

1. Because the autocorrelogram sampled at 2000Hz can have high variability across samples, we fitted a polynomial to the autocorrelogram. We determined the order of the polynomial fit with a cross-validation procedure, which prevented overfitting. In this cross-validation procedure, trials were divided into two non-overlapping sets, which were the “training” and the “test” set. Polynomials of orders from 5 to 40 were fitted on the training set. We selected the polynomial order that yielded the smallest error on the test set. Finally, we fitted a polynomial of the selected order to the autocorrelogram that was computed based on all the trials.
2. Because the autocorrelograms often had sidelobes due to rhythmic firing, we dampedened this rhythmicity by convolving the polynomial fits with a moving-average filter. The length of the moving-average filter was equal to the average length of the gamma cycle, which was determined per monkey separately (15ms in monkey J and 26ms in monkey L). The moving-average filter was only applied to samples beyond 8ms.
3. We determined the time at which the smoothed polynomial-fit reached a global peak within 0-60ms ([Figure 2E](#)). In addition, we determined the time at which the smoothed autocorrelogram reached a global peak within 0-12ms ([Figure S2C](#)).
4. We defined two additional measures of burst-propensity. The first measure of burst-propensity was comparable to a Z-score, and was defined as $Z = ((x_1 - \bar{x}_2) / \sqrt{s_1^2 + s_2^2})$. Here, x_1 was the maximum value of the polynomial fit within 5ms, and \bar{x}_2 was the minimum value within 5-10ms. These values were associated with standard errors s_1 and s_2 , which were obtained through a bootstrapping procedure. The value of this measure is shown in [Figure 2E](#). We defined another measure of burst-propensity by comparing the maximum value of the polynomial fit within 0-5ms, x_1 , with the maximum value within 8-10ms, x_2 . This measure was defined as $\log_{10}(x_1 / x_2)$ and is shown in [Figures S2B](#) and [S2C](#).
5. We identified two non-overlapping clusters of NW neurons based on the global peak-time in the autocorrelogram ([Figure 2E](#)). As an additional criterion for NW-Burst neurons, we required them to have a burst-modulation of at least 20%. This criterion was not reached by two neurons ([Figure S2B](#)), which were not further analyzed. Inclusion of these two neurons into the NW-Burst population did not qualitatively alter the results. A few neurons had peaks in the autocorrelogram within 5ms, and a relatively high burst-modulation score ([Figure S2B](#)). However, their autocorrelograms did not reach a global maximum within 5ms when considering the entire 60ms interval ([Figure S2C](#)). We considered the classification of these neurons as unclear and included them neither into the NW-Burst nor in the NW-Nonburst population.

Other Measurement of Burst-Propensity

The total fraction of burst-spikes was computed based on the inter-trial-interval distribution. We counted the number of spikes either between 0.008ms and 3.5ms (short burst intervals), or between 0.008ms and 6ms (long burst intervals). We defined the ratio a/b , where a was the number of burst spikes and b the total number of spikes.

To compute the correlation between burstiness in the pre-stimulus and the stimulus period ([Figure S2 FigBurstingRatesSI](#)), we defined the burst-propensity based on the autocorrelogram. This avoids potential biases due to differences in discharge rates ([Senzai et al., 2019](#)). The burst-propensity was defined as the ratio $(a - b)/(a + b)$. Here, a was the average value of the normalized autocorrelogram either between 0.0008s and 3.5ms (short bursts), or between 0.0008s and 6ms (long bursts). The variable b was the average value of the normalized autocorrelogram between 0.008 s and 0.1 s. We also used this measure of burst-propensity for the correlation with spike-LFP phase-locking values.

Quantification of Spike-LFP Phase-Locking

To compute spike-LFP phase-locking, we determined the phase of each spike relative to the LFP recorded from the other electrodes. To remove line noise, we filtered the LFP signals with a two-pass 4th order Butterworth bandstop-filter (49.5-50.5Hz). We then averaged the LFP signals across the other electrodes, which was justified because of their high coherence. We computed the “spike-LFP phase” in two different ways:

In the first approach, we computed the wavelet transform of the LFP snippet around each spike, using a constant number of cycles (9) per frequency (as in ([Vinck et al., 2013a](#))). The advantage of this method is that it allows for a comparison of spike-LFP phase-locking between different frequencies, similar to the spike-field coherence. The disadvantage is that many LFP cycles are used to determine the spike-LFP phase. This could lead to an underestimation of spike-LFP phase-locking, because the probability of a spike should not be influenced by LFP fluctuations that are far away in time.

The second method addressed this problem and consisted of the following steps:

1. We band-pass-filtered the LFP in a relatively broad frequency-band with a 3-th order, two-pass Butterworth filter (40-90Hz in monkey J, 25-55Hz in monkey L).

2. We computed the Hilbert-transform of the band-pass filtered signal and determined the instantaneous phase.
3. We detected gamma cycles as follows: First, we detected all the zero-crossings of the instantaneous phase, which occur in the neighborhood of peaks in the band-pass filtered signal. For each k -th zero-crossing, we examined whether the angular velocity of the phase was positive for all time points between the $k - 1$ -th to the $k + 1$ -th zero-crossing. If this was not the case, then there was a “phase-slip” in which the instantaneous frequency became negative. Otherwise, we detected the nearest peak in the band-pass filtered signal relative to the k -th zero-crossing of the phase. We then measured the duration of the gamma cycle as the time from the current peak to the next peak in the signal.
4. We ran the same cycle selection-procedure on the pre-stimulus period, in which narrow-band gamma-band oscillations are virtually absent. For the pre-stimulus period, we obtained the mean μ_{pre} and standard deviation σ_{pre} of the distribution of amplitudes. These amplitudes were measured as the peak-to-valley distance of the gamma cycle (Atallah and Scanziani, 2009). A cycle in the stimulus period with amplitude A was only selected if $(A - \mu_{pre})/\sigma_{pre} > 1.63$ (which would be the cut-off for a one-sided t test at $P < 0.05$).
5. We defined the gamma phase as t/T , where t was the time from the peak of the gamma cycle, and T the time to the next peak.

After computing the spike-LFP phases, we estimated phase-locking with the pairwise-phase-consistency (PPC) (Vinck et al., 2012, 2010b). Specifically, we used the PPC1 measure defined by Vinck et al. (2012). The PPC1 takes all pairs of spikes-LFP phases from separate trials and computes the average consistency of phases across these pairs. It is not affected by mean discharge-rates and history effects like bursting (see STAR Methods) (Vinck et al., 2012). The bias due to discharge rates is removed by the pairwise computation (Vinck et al., 2012). The bias due to history effects is removed by considering only pairs of spike-LFP phases from separate trials (Vinck et al., 2012). Thus, PPC values can be directly compared between neuron types with varying discharge rates and burst-propensity. Because phase-locking estimates can have a high variance for low spike counts, we computed PPC values only for neurons that fired at least 50 spikes (Vinck et al., 2013a).

To compute spike-triggered averages of the LFP, we first Z-transformed the LFP signals such that they had unit standard deviation. The STA was defined as the average Z-scored LFP signal across spikes.

Orientation and Direction Tuning

We measured orientation-tuning with the orientation-selectivity-index (OSI). The OSI was defined as in Womelsdorf et al. (2012): The mean discharge rates, r_m (spikes/sec), were determined for each m -th stimulus orientation. The angle of the stimulus orientation θ_m was a circular variable that ranged between 0 and 2π radians. The discharge rates were normalized as $w_m = r_m / \sum r_m$. The OSI was defined as

$$R = \left| \sum_{m=1}^8 w_m \exp(i\theta_m) \right|. \quad (1)$$

This quantity can be understood as the resultant vector-length, which is obtained by adding eight vectors with angle θ_m and magnitude w_m . For the direction-selectivity index (DSI), the variable θ_m represented the stimulus direction and w_m was the discharge rate for the m -th stimulus direction. We have previously shown that the OSI estimate is positively biased (Womelsdorf et al., 2012). This bias decreases as the discharge rate or the trial count increase (Womelsdorf et al., 2012). Thus, uncorrected OSI (and DSI) values are typically high for neurons with low discharge-rates (Womelsdorf et al., 2012). We estimated this bias by shuffling the discharge rates across trials, and computing R for the shuffled data (Batista-Brito et al., 2017). We then computed the average value of R across 1000 shuffling iterations, and subtracted the bias estimate from the observed value of the OSI (or DSI) (Batista-Brito et al., 2017).

Simple versus Complex-Cell Modulation

We used the following procedure to determine the extent to which V1 neurons had simple or complex receptive-fields: For each neuron, we estimated the discharge rate as a function of time by convolving the spike train with a Gaussian kernel (40ms length, standard deviation 10ms). “spike-density function”). This spike-density function was computed only for the preferred stimulus-orientation. We then fitted a sinusoid with the temporal frequency of the drifting gratings to this spike-density function. We computed this fit for the period starting >200ms after stimulus onset, in order to avoid the initial stimulus transient. We also estimated the bias of the sinusoid fit, B , by fitting a sinusoid which was shifted by a random phase in each trial. A modulation term $F1$ was defined as the difference between the amplitude A and the bias B , $F1 = A - B$. If $F1 < 0$, then we set $F1 = 0$. To measure simple versus complex-cell modulation, we computed the measure $M = (F1 - F0)/(F0 + F1)$. Here, $F0$ is the mean elevation of firing above baseline. Note that this definition is different from the $F1/F0$ ratio that has been used in other studies (Martinez and Alonso, 2003). However, the normalization in the denominator makes M robust against outliers and also well-behaved when $F0$ is close to zero. Previous studies have used $F1/F0 = 1$ as a cut-off point to define simple cells. With the definition of M , the equivalent cut-off point for simple cells would be $M = 0$.

Correlation between Firing Rate and Phase-Locking across Stimuli

We computed the correlation between firing rate and phase-locking across the 16 stimulus directions as follows (Figure 8): For each neuron, we determined discharge rates for each of the 16 different stimulus-directions. These discharge rates were normalized by dividing by the maximum discharge-rate, such that the normalized discharge-rates were bound by 0 and 1. We also computed the gamma phase-locking value (PPC) for each of the 16 stimulus directions separately. The 16 gamma phase-locking values (PPC) were then predicted from the 16 corresponding values of the discharge rate. Because the variance of the phase-locking estimate (PPC) decreases as a function of the spike count, we used a weighted linear-regression model. In this model, the influence of an observation on the regression fit was proportional to the inverse of the variance. The variance of the PPC was estimated with a bootstrapping procedure, in which we bootstrapped over trials.

Statistical Testing

We used permutation testing for statistical comparisons between different neuron types (Maris and Oostenveld, 2007). First note that the two monkeys may systematically differ in a certain variable (e.g., the OSI), and that there might be more neurons of a certain type in one monkey. This could potentially bias our analyses when comparing neuron types. We addressed this problem as follows: For a comparison between values of X (representing any variable) between two neuron types, we Z-scored the values of X across the two neuron types per monkey separately. This ensured that the mean of the Z-scored variable was identical between the two monkeys. We then pooled the Z-scores across the two monkeys. As an alternative testing strategy, we also computed the difference in X per monkey separately, and averaged the difference score across the two monkeys. This yielded qualitatively similar results. For permutation testing, we randomly permuted the labels of the two neuron types under consideration. We then constructed a permutation distribution for differences between two neuron types. We computed the p value by comparing the observed difference between two neuron types with the permutation distribution. We corrected for multiple comparisons using an FDR correction (5% false positive rate, correction for dependent tests). The permutation test does not make assumptions about the shape of the distribution of the data. Error bars in all figures correspond to standard errors of the mean. Statistics are described in the Results and figure legends.

DATA AND CODE AVAILABILITY

The open-source MATLAB toolbox Fieldtrip (Oostenveld et al., 2011) was used for data analysis. Data and custom MATLAB analysis scripts are available upon reasonable request from Martin Vinck (martin.vinck@esi-frankfurt.de).